Early exposure to broadly neutralizing antibodies triggers a switch from progressive disease to lasting control of SHIV infection

Rajat Desikan[1†‡*], Rubesh Raja[1†], Narendra. M. Dixit[1,2*]

[1]Department of Chemical Engineering, Indian Institute of Science, Bengaluru, India, 560012.

[2]Centre for Biosystems Science and Engineering, Indian Institute of Science, Bengaluru, India, 560012.

***Correspondence:**

Rajat Desikan, rajatdesikan@gmail.com

Narendra M. Dixit, narendra@iisc.ac.in

†These authors contributed equally to this work.

‡Present address: Akamara Biomedicine Private Limited, Ist Floor, No. 465, Patparganj Industrial Area, Delhi, India. 110092.

Keywords: Passive immunization | HIV/SHIV | functional cure | T cells | broadly neutralizing antibodies | bNAb therapy | mathematical modeling | viral dynamics

Document statistics:

Title: 129 characters | Abstract: 250 words | Importance: 120 words | Text: ~48000 characters including figure captions and references | Figures: 6 | References: 58

Supplementary text: 1 | Supplementary figures: 11 | Supplementary tables: 10 | Supplementary database: 1

Abstract

Passive immunization with broadly neutralizing antibodies (bNAbs) of HIV-1 early in infection has been shown recently to elicit long-term viremic control in a majority of SHIV-infected macaques treated, raising hopes of a functional cure of HIV-1 infection. The mechanisms underlying this control remain unclear. Untreated infection typically leads to progressive disease. We hypothesized that viremic control represents an alternative but rarely realized outcome of the infection and that early bNAb therapy triggers a dynamical switch to this outcome. To test this hypothesis, we developed a mathematical model of viral dynamics with bNAb therapy and applied it to analyze recent *in vivo* data. We let bNAbs increase viral clearance and antigen cross-presentation in a dose-dependent manner. Model predictions fit quantitatively the entire time course of viral load changes in macaques that achieved lasting control, giving us confidence in the model. Steady-state model predictions showed bistability, indicating two distinct outcomes of infection. The first had high viremia, weak cytotoxic T lymphocyte (CTL) responses, and high CTL exhaustion, marking progressive disease. The second had low viremia, strong CTL responses, and low CTL exhaustion, indicating lasting viremic control. Early bNAb therapy lowered viremia, which also limited CTL exhaustion, and improved CTL stimulation via cross-presentation. Post bNAb therapy, viremia resurged but in the presence of a primed CTL population, which eventually controlled the infection. Antiretroviral therapy suppresses viremia but does not enhance CTL stimulation, which limits its ability to elicit post-treatment control. Our model suggests bNAb-based intervention protocols for maximizing functional cure of HIV-1 infection.

Importance

Antiretroviral therapy (ART) for HIV-1 infection is life-long. Remarkably, a recent study showed that 3 weekly doses of HIV-1 broadly neutralizing antibodies (bNAbs) soon after infection kept viral levels controlled for years in macaques. If translated to humans, this bNAb therapy may elicit a functional cure of HIV-1 infection, eliminating the need for life-long treatment. How early bNAb therapy works in macaques remains unknown. Here, we elucidate the mechanism using mathematical modeling and analysis of in vivo data. Early bNAb therapy suppresses viremia, reduces cytotoxic T lymphocyte (CTL) exhaustion, and enhances antigen uptake and CTL stimulation, which collectively drive infection to lasting control. Model predictions fit the complex in vivo data quantitatively and suggest new avenues to optimize bNAb-based interventions.

Introduction

Current antiretroviral therapies (ART) for HIV-1 infection control viremia in infected individuals but are unable to eradicate the virus (1). A reservoir of latently infected cells, which is established soon after infection (2), escapes drugs and the host immune response (3), is long-lived (4, 5), and can reignite infection following the cessation of therapy (6), presents the key obstacle to sterilizing cure. Efforts are now aimed at eliciting a "functional cure" of the infection, where the virus can be controlled without life-long treatment even though eradication is not possible (7). That functional cure can be achieved has been demonstrated by the VISCONTI trial, where a subset of patients, following early initiation of ART, maintained undetectable viremia long after the cessation of treatment (8). A limitation, however, is that the subset that achieves post-treatment control with ART is small, 5-15% of the patients treated (9). In a major advance, Nishimura *et al.* (10) found recently that early, short-term passive immunization with a combination of two HIV-1 broadly neutralizing antibodies (bNAbs) elicited lasting control of viremia in 10 of 13, or nearly 77%, of SHIV-infected macaques treated. This high success rate raises the prospect of achieving functional cure in all HIV-1 infected individuals using short-term bNAb therapy. Efforts have been initiated to develop immunotherapies that may further improve response rates in primate models (11-14) and to translate them to humans (15-17).

Devising passive immunization protocols that would maximize the chances of achieving functional cure requires an understanding of the mechanism(s) with which early, short-term passive immunization with bNAbs induces sustained control of viremia. Nishimura *et al.* (10) argue that the control they observed, lasting long (years) after the administered bNAbs were cleared from circulation (weeks), was due to the effector function of cytotoxic $CD8^+$ T lymphocytes (CTLs) because transient suppression of CTLs, using anti-CD8 antibodies (Abs), well after the establishment of control resulted in a temporary surge of viremia. How short-term bNAb therapy leads to sustained CTL stimulation, and therefore lasting viremic control, remains unknown (15).

Here, we propose a dynamical systems-based role of bNAbs in eliciting lasting control. We hypothesized that lasting viremic control is a distinct but rarely realized outcome of HIV-1 infection and that early, short-term bNAb therapy triggers a switch in disease dynamics that significantly increases the likelihood of realizing this outcome. To test this hypothesis and to elucidate the mechanisms with which bNAbs orchestrate this switch, we constructed a

mathematical model of HIV dynamics under bNAb therapy and applied it to analyse recent *in vivo* data.

Results

Mathematical model of viral dynamics with passive immunization

We constructed a mathematical model that considered the within-host dynamics of populations of uninfected target $CD4^+$ T cells, productively infected cells, free virions, effector CTLs, and administered bNAbs (Figure 1). Where necessary, we also considered latently infected cells (see below). The dynamics in the absence of bNAbs were similar to those in recent models of viral dynamics that include effector cells (18-20). Briefly, uninfected target cells get infected by free virions to yield productively infected cells, which in turn produce more free virions. CTLs are stimulated by infected cells and could become exhausted by sustained antigenic stimulation. Activated CTLs kill infected cells. We modified these processes based on the known effects of bNAbs (15, 21): bNAbs opsonize free virions, preventing them from infecting cells and enhancing their clearance (22-24). Opsonized virus can also be taken up by immune cells, particularly macrophages, and via processes now being unraveled improve antigen presentation and increase infected cell death (25-28). Thus, we let bNAbs 1) enhance the clearance of free virions and 2) increase CTL activation, via enhanced antigen uptake, both in a dose-dependent manner. The enhanced viral clearance, which results in a reduction in viremia, was assumed to subsume the effect of virus neutralization (see Methods). By lowering antigen levels, bNAbs could reverse CTL exhaustion.

ART was assumed to reduce the productive infection of target cells. Anti-CD8 Abs were assumed to reduce the CTL population and compromise host effector functions for a duration corresponding to the residence time of the depleting Abs in circulation.

We constructed equations to describe the resulting dynamics and solved them using parameter values representative of SHIV infection of macaques (Methods and Text S1).

Model predictions fit in vivo data

To test whether the model accurately captured the underlying dynamics of infection and the influence of bNAbs, we applied it to describe the viral load changes reported in Nishimura *et al.* (10) where 3 weekly infusions of a combination of two HIV-1 bNAbs,

3BNC117 and 10-1074, starting from day 3 post SHIV challenge were administered. We considered the 10 "responder" macaques who showed no significant decline in $CD4^+$ T cell counts and included 6 with undetectable post-treatment set-point viremia ($<10^2$ copies/mL), termed "controllers", and 4 with detectable but low post-treatment set-point viremia ($<10^3$ copies/mL). We also considered 10 untreated macaques in the study with viral load measurements reported during the acute phase of infection. Where available, we fixed model parameter values from previous studies (Text S1 and Table S1). We estimated the remaining parameters by using non-linear mixed effects modeling to simultaneously fit viral load data (Figure 2) and bNAb concentrations (Figure S1) in the responder macaques and viral load data in the untreated macaques (Figure S2). The model provided good fits to the data, yielding population-level parameter estimates (Table S2) and parameter estimates yielding best-fits to individual macaques (Tables S3 and S4). The population parameters compared well with previous estimates, wherever available (Text S1).

The viral dynamics during and post bNAb therapy was complex and could be divided into the following phases (Figure 2). Viremia dropped post the acute infection peak to undetectable levels ($<10^2$ copies/mL), where it remained until the administered bNAb level in circulation declined to a point where its ability to control viremia was lost (Phase I in Figure 2a). Viremia then resurged to an elevated level ($\sim 10^5$ copies/mL), well above the acute infection peak ($<10^4$ copies/mL), but subsequently declined spontaneously to a low (10^2-10^3 copies/mL) level (Phase II), where it remained for the rest of the duration of follow-up (>3 years; Phase III).

Following the administration of anti-CD8 Abs, several months after the establishment of control, viremia immediately resurged to high levels again, but was eventually controlled (Phase IV) in 5 of 6 macaques thus treated (Figure 2). One macaque (DFIK) lost control following the administration of anti-CD8 Abs and reached a high viral load set-point, akin to untreated macaques.

The ability to describe these complex viral load changes during and post bNAb therapy quantitatively gave us confidence in our model. We applied our model next to elucidate the mechanistic origins of the observed long-term viremic control.

Viremic control is a distinct outcome of infection

We hypothesized, based on the two outcomes, progressive disease vs. viremic control, achieved following bNAb therapy as well as CD8 depletion, that lasting control observed with early bNAb therapy was a distinct steady state of the system. This hypothesis of bistability, or the existence of two distinct stable steady states, is consistent with a previous analysis of post-treatment control with ART (18) and may be a general feature of the interactions between Ag and CTLs (20). Indeed, solving our model equations (Methods), we identified two underlying stable steady states (Figure 3). The first had high viremia, relatively high levels of CTL exhaustion and relatively weak CTL effector function, marking chronic infection leading to progressive disease. The second had low viremia, relatively low levels of CTL exhaustion and relatively strong CTL effector function, indicating lasting control. These states existed over wide ranges of parameter values (Figure S3).

To indicate the two steady states for given parameter values, we use red and blue filled squares, respectively, in all the figures. The two stable states were separated by an unstable steady state of intermediate viremia, and intermediate CTL stimulation and/or exhaustion levels. In addition, an uninfected steady state existed that was also unstable.

Early, short-term bNAb therapy switches the outcome to viremic control via pleiotropic effects

When a new infection occurs, viremia rises significantly during the acute infection phase and achieves high levels typically before a CTL response is mounted (29). The CTL response thus lags and is dominated by the virus. If left untreated, the high viremic state, leading to progressive disease, is realized. This behaviour is consistent with observations of untreated macaques challenged with SHIV (30, 31), which our model recapitulates (Figure S2; red lines in Figure 4). The model predicts that following the initial transients, a high viremia, a high level of exhaustion, and a weak CTL response result.

Our model also predicts that early bNAb therapy drove the infection to the state of lasting viremic control (blue lines in Figure 4), in agreement with the observations in Nishimura *et al.* (10). Further, our model predicts that pleiotropic effects of bNAbs were involved in orchestrating this transition: During acute infection, bNAbs suppressed the viremic peak by enhancing viral clearance. The lower viremia would limit CTL exhaustion. Further, bNAbs would increase antigen presentation and CTL stimulation. When the level of the administered bNAbs in circulation diminished, viremia resurged but would now do so in the presence of a

primed CTL population, which would be larger and/or less severely exhausted than in untreated macaques (Figure 4c-e). The primed CTL population was able to control the infection in our predictions. Further, based on our predictions, when the CTL level is substantial before bNAb clearance, viremia would rise minimally post bNAb therapy, as observed with the macaque DEWP (Figure 4). When the CTL level is smaller, viremia would resurge post bNAb therapy, but the limited CTL exhaustion together with increased CTL stimulation from the residual bNAbs would trigger a strong enough CTL response to reassert control, akin to the observations with the macaque MVJ (Figure 4).

We may construe the rise in viremia post treatment as arising from a new infection of the macaque but under conditions where the CTL population is primed and thus has a head start over the virus. Indeed, our model calculations of the hypothetical scenario where a higher CTL population existed at the time of viral challenge showed spontaneous control (Figure S4).

Similarly, our model predicts that suppression of CTLs up to a threshold after the establishment of control allowed resurgence in viremia but restored control, whereas suppression beyond the threshold sacrificed control and drove infection to the former, high viremic fate (Figure 2), explaining the difference between the controller macaques who reasserted viremic control following the transient rise in viremia upon the administration of anti-CD8 Abs and the one controller macaque that failed to reassert control and transitioned to the high viremic state (10). Note that the threshold can vary across macaques and corresponds, in our model, to the unstable boundary separating the stable states of viremic control and progressive disease (Figure 3).

When we repeated our analysis without either enhanced clearance of virus or upregulation of antigen presentation by bNAbs, our model failed to capture the observed viral load data robustly (Figure S5 and Table S5). Specifically, when we fit our model without bNAb-induced upregulation of antigen presentation, the resulting best-fit parameters were such that a 1 $\log_{10}$ lower viral inoculum resulted in the loss of viral control, which cannot be justified. No macaques administered lower inoculum sizes ($TCID_{50}$ of 100; see Figure 2) failed treatment. It is reasonable therefore to assume that for a macaque that achieved lasting control with the lower inoculum size ($TCID_{50}$ of 100), lowering the initial viral load further by a factor of 10 should not result in a loss of control. But that is what a model without bNAb-induced upregulation of antigen presentation predicted (Figure S5). On the other hand, a model without enhanced viral clearance failed to fit the data (Figure S5). The rapid clearance of the virus, which lowered viremia and reversed CTL exhaustion, together with increased Ag uptake,

which led to enhanced CTL stimulation, thus resulted in the lasting control of viremia elicited by early, short-term bNAb therapy.

bNAbs have an advantage over ART

If ART were used instead of bNAbs, for a duration equivalent to the time over which the administered bNAbs were in circulation, viral load quickly became undetectable during treatment in our model but rebounded to high levels post treatment (Figure 5), consistent with the 3 macaques administered ART in Nishimura *et al.* (10). While both bNAb therapy and ART limited viremia (Figures 4a, 4b, 5a) and would thus prevent CTL exhaustion (Figures 4e, 4f, 5c), bNAb therapy would additionally increase antigen presentation and CTL stimulation (Figures 4b, 4d, 5b). The resurgence in viremia post the cessation of ART would thus be akin to *de novo* infection, which typically reaches the high viremic fate. Only in the rare individuals in whom the latent reservoir is sufficiently small is this rise in viremia small enough for the CTL population to catch up and establish control, explaining the critical role of the size of the latent reservoir in post treatment control with ART (18). The primed CTL population following bNAb therapy, in contrast, drove the system to viremic control. Because of their pleiotropic effects, bNAbs thus have a significant advantage over ART, explaining their much higher success rate in achieving lasting control.

Strategies to maximize the impact of bNAb therapy

The above difference between ART and bNAb therapy suggests that an optimal window of bNAb efficacy may exist for eliciting lasting control: Too low an efficacy would fail to achieve adequate viremic control, whereas too high an efficacy would render bNAbs similar to ART and forego their effect on upregulating the CTL response. To test this, we explored our model predictions over a wide range of maximum bNAb concentrations and the bNAb half-lives, which would define the overall bNAb efficacy, and which varied substantially across macaques (10) (Figure S1 and Table S3).

Our model predicts, indeed, that for any bNAb half-life, a window of the maximum bNAb concentration exists within which viremic control is established and outside which the high viremic, progressive state results (blue region in Figure 6a). When the concentration is below the window (lower red region in Figure 6a), the bNAb therapy is not potent enough to control the infection (orange lines in Figure 6e-f). On the other hand, when the concentration

is above the window (upper red region in Figure 6a), bNAb therapy is too intense and behaves like potent ART; the drastic reduction in viremia leaves few activated CTLs behind to control the infection post therapy (brown lines Figure 6b-d).

One way to achieve control is to ensure that the maximum bNAb concentration lies in the admissible window. Indeed, increasing the dosage in the former (purple lines in Figure 6e-g) and decreasing it in the latter scenario would lead to lasting control (dark green lines in Figure 6b-d). Deciding whether to increase or decrease dosage, however, may be difficult when the admissible window is not known *a priori*.

Promisingly, our model predicts that the admissible window widens with increasing bNAb half-life (Figure 6a). The widening is due both to a decrease of the lower limit and an increase of the upper limit of the window. Thus, in either scenario of failure above, increasing the bNAb half-life would lead to lasting control (pink and light green lines in Figure 6b-g). Our model predicts that increasing half-life while keeping the maximum concentration fixed leads to faster viral load decline because of the more potent resulting overall bNAb action, making bNAb therapy more like ART in its effect on the viral load. However, it would also increase the overall antigen uptake and presentation and hence CTL stimulation, making it different from ART in its effect on the CTL response. For instance, the residual bNAbs during the post-treatment rise in viremia would limit the extent of the rise, reducing the level of CTL exhaustion and increasing CTL stimulation, and help reestablish control (compare purple and orange lines in Figure 6e-g). In our calculations, the effects of bNAbs on CTLs outweighed their effect on viral load decline, leading to better lasting control with increasing half-life. Indeed, beyond a critical half-life (~17 d in Figure 6a), a sufficiently robust CTL response is predicted to be built up regardless of the maximum bNAb concentration, because viral clearance saturates and becomes independent of the latter concentration beyond this threshold. The admissible window then ceases to have an upper bound. In this regime, failure would imply inadequate bNAb efficacy (lower red region in Figure 6a), so that increasing bNAb concentration and/or half-life would ensure lasting control. Interestingly, the bNAbs, 3BNC117-LS and 10-1074-LS, engineered to have longer half-lives, appear to fall in the latter regime, when we used parameter values corresponding to the population means (Table S2; Figure 6a), suggesting that and explaining why their use may lead to better lasting control.

We emphasize that we have used bNAb concentrations and half-lives as surrogate markers of efficacy. Individuals with similar drug pharmacokinetic characteristics may experience widely varying efficacies, suggesting differences in their pharmacodynamic

characteristics. Indeed, when we fit our model of bNAb pharmacokinetics to data from the 3 non-responder macaques in Nishimura *et al*. (10), significant differences compared to responders were not apparent (Figure S7; Table S6). Note that the admissible window varies substantially with parameter values and hence is expected to be macaque specific (Figure S6). Thus, inter-patient variations would thus have to be accounted for, through studies over much larger populations, before our predictions can be used to arrive at quantitative strategies.

Nonetheless, we expect our qualitative finding of an admissible window of bNAb efficacies to hold. Thus, tuning the dosage to ensure that the maximum bNAb concentration lies in the admissible window and/or increasing the bNAb half-life would maximize the chances of achieving lasting control.

Discussion

The recent success of passive immunization with bNAbs in eliciting functional cure of HIV-1 infection can potentially revolutionize HIV-1 care (10-17). In this study, using mathematical modelling and analysis of *in vivo* data, we present a dynamical systems view of the infection that explains how early exposure to bNAbs induces lasting viremic control and suggests strategies to maximize the impact of bNAb-based therapies.

Our study makes significant advances in understanding functional cure as well as the influence of bNAbs. Nishimura *et al.* have argued that CTLs were responsible for the lasting control induced by early bNAb therapy in the macaques in their experiments (10). They do not explain, however, how the CTL response could be sustained years after treatment (15). Our study provides an answer. Broadly, the virus exerts competing influences on CTLs, both stimulating them and triggering their exhaustion. At the same time, CTLs suppress viremia. One outcome of these interactions is progressive disease, where the virus suppresses the CTL response. The other is lasting control, where the virus is suppressed by CTLs. Importantly, the latter is a ‘stable’ steady state, where a balance is achieved between CTL stimulation and viremic control. A higher viremia than what is present in this steady state would increase CTL stimulation, which in turn would suppress viremia. Similarly, a lower viremia would reduce CTL stimulation and allow viremia to rise. The stable steady state ensures that the corresponding level of CTL stimulation and viremia are maintained long after treatment.

From a dynamical systems viewpoint, both progressive disease and lasting control are states ‘intrinsic’ to the system. Interventions, with either ART or bNAbs, serve to alter the

propensity with which the two states are realized. Once realized, the states are self-sustaining. In untreated infection, rapid viral growth induces significant CTL exhaustion and leads to progressive disease. ART suppresses viremia and would therefore at least in part reverse exhaustion. (Recent studies have argued that CTL exhaustion may not be fully reversible (33).) However, because successful ART can completely block viral replication, the absence of antigen would eventually cause the activated CTL population to fade. When viremia rises post treatment, if the activated CTL population has faded significantly, the dynamics would mimic *de novo* infection leading to progressive disease. The resurgence of viremia post ART is due to the reactivation of latently infected cells. When the latent pool is small, this reactivation may lead to low viremia, which can stimulate CTLs and reach the state of viremic control, described above. Indeed, a model to explain post-ART control found a crucial role of the latent reservoir (18). In contrast, bNAbs additionally stimulate CTLs by enhancing antigen presentation. Although this remains to be proven experimentally, without this effect, our model was not consistent with data. When viremia rises post bNAb therapy, it then would encounter a primed CTL population, which would drive the system to the state of viremic control. Unless intense bNAb therapy completely halts active viral replication, akin to ART, the establishment of control is less likely to be sensitive to the latent pool size. Indeed, our model fit the macaque data without considering latently infected cells. bNAbs would therefore achieve lasting control in a far greater percentage of the population treated. As expected, whereas ART leads to control in 5-15% patients, Nishimura *et al.* found control in ~77% macaques treated with bNAbs. Future studies may assess the latter percentages in humans.

In two recent studies, the same bNAb combination therapy used by Nishimura *et al.* (10) was extended to humans who were either untreated or on treatment interruption following viral suppression with ART (16, 17). The bNAb therapy was well tolerated and suppressed viremia akin to macaques. When viremia rose following the clearance of the administered bNAbs, the patients were (re)started on ART, precluding the possible establishment of spontaneous long-term control observed in the responder macaques in Nishimura *et al.* (10).

Our study suggests avenues to maximize the impact of bNAb therapy. Previous studies either examined the steady states alone (18) or short-term viral load changes following exposure to bNAbs (24). Going beyond, our study captures the entire time course of viral load changes leading to lasting control, resulting in a more comprehensive understanding of functional cure. Our model predicts that increasing bNAb concentration and half-life, which are both expected to increase treatment efficacy, could have vastly different effects. For typical

bNAb half-lives, our model predicts that a window of maximum bNAb concentrations exists within which lasting control would result. Thus, increasing bNAb concentration beyond the window would be counterproductive. Accurate estimation of the admissible window, which may vary across individuals, may be difficult *a priori*. On the other hand, the admissible window widens with increasing half-life and eventually becomes unbounded above. Thus, increasing half-life would invariably improve the chances of achieving lasting control. Sustained bNAb exposure can be achieved with more frequent dosing. Alternatively, bNAbs engineered to have longer half-lives (32) could be employed. While the studies on bNAb engineering have focused on minimizing the dosing frequency, our study suggests that increased bNAb half-life has a more fundamental advantage in ensuring lasting viremic control. Once future studies quantify inter-patient variability in bNAb efficacies, our model could be applied to devise suitable dosing protocols and to inform efforts to engineer bNAb half-lives (32).

Through pleiotropic effects, bNAbs tilt the balance of the competing interactions between the virus and CTLs in favour of CTLs. It follows that other strategies that similarly tilt the balance may also elicit functional cure. For instance, immune checkpoint inhibitors can prevent CTL exhaustion during infection (34). CTLs can also be stimulated using vaccines (35). Our model predicts that a primed CTL population at the time of viral challenge may prevent the infection from reaching the high viremic, progressive state and drive it instead to lasting viremic control, indicating a potentially favourable outcome of preventive T cell vaccines. Stimulating CTLs using vaccines has been shown to suppress viral replication and lower the set-point viremia (36, 37), but several additional design challenges must be overcome, including the need to stimulate CTLs early enough and, interestingly, prevent CTL exhaustion due to the vaccine (38), for the successful deployment of T cell vaccines (39). Future studies may test whether these latter strategies, independently or in combination with bNAbs, can improve the chances of achieving functional cure.

Our study has parallels in other viral infections and cancers. Post-treatment cure has been seen recently with hepatitis C virus infection following therapy with direct acting antiviral agents (40). Although the underlying mechanisms are yet to be established (41-43), one possibility is the reversal of immune exhaustion due to the reduction in the viremia during treatment, which could allow a rejuvenated CTL response to eliminate the virus post-treatment (41). The interactions between Ag and CTLs in our model are consistent with a general dynamical motif posited recently to explain the predominant outcomes of viral infections,

namely, clearance, persistence, and host-mortality due to immunopathology (20). Interventions that modulate these interactions have been argued to be able to alter the outcomes realized (20), as we suggest here. Finally, long-lasting anti-tumor CTL responses have been observed following limited exposure to tumor-specific Abs administered through passive immunization, a phenomenon termed the vaccinal effect (44), which has been shown to occur due to improved uptake of opsonized Ag by APCs and subsequent cross-presentation to CTLs leading to the generation of memory. We speculate that the vaccinal effect may also arise when the tumor is not completely eliminated as an alternative steady state of the dynamical interactions between tumor Ag and CTLs, mirroring our findings here, and could lead to long-term tumor control. Furthermore, immune checkpoint inhibitors, which act by partially reversing CTL exhaustion (45), may improve the chances of achieving such control.

Although our model is complex, it is restricted to the essential effects of bNAbs. Following the observation of Nishimura *et al.* (10) that there was no significant generation of anti-gp120 Abs in controllers, we ignored the ability of bNAbs to upregulate the humoral response (46). Our study is thus conservative in its assessment of the influence of bNAbs. We did not consider data from non-responder macaques, where functional cure is not established and $CD4^+$ T cell counts gradually decline. Describing the entire course of HIV infection from the acute phase to AIDS using a single model has been a long-standing challenge. Only recently, a model invoking pyroptosis has been developed for the purpose (47) and may have to be integrated into our model to describe the gradual $CD4^+$ T cell decline leading to AIDS (48). Not enough data is available currently, however, to estimate the additional parameters that would then be introduced. Nonetheless, the essential idea of the two distinct fates of infection and the ability of bNAbs to induce a switch between them is expected to hold because pyroptosis determines how $CD4^+$ T cell counts decline *after* the establishment of the high viremic state and, also, it is expected not be a significant force when viremia is controlled. We subsumed the effects of virus neutralization and antibody-dependent cellular cytotoxicity (24) into the enhanced viral clearance and infected cell loss following bNAb therapy. Finally, we did not consider viral evolution and resistance to bNAbs, recognizing that the most controllers in Nishimura *et al.* (10) saw no resistance. Future studies on larger populations and with other combinations of bNAbs may determine whether resistance must be accounted for in defining optimal treatments, especially for use during chronic infection where viral diversity is likely to be large (49).

In summary, our study presents the first quantitative description of viral dynamics following passive immunization with HIV-1 bNAbs; captures *in vivo* data; elucidates the mechanisms with which early, short-term bNAb therapy establishes lasting viremic control of SHIV infection; and presents avenues to maximize the success rate of bNAb therapies in inducing functional cure of HIV-1 infection.

Methods

We constructed the following equations to describe the viral dynamics depicted schematically in Figure 1.

$$\frac{dT}{dt} = \lambda_T - d_T T - \beta V T \tag{1}$$

$$\frac{dI}{dt} = \beta V T - \left(d_I + mE\right) I \tag{2}$$

$$\frac{dV}{dt} = pI - (c + A)V \tag{3}$$

$$\frac{dE}{dt} = \frac{\left(\rho + k_E E\right)\left(I + fAV\right)}{\phi_1 + I + fAV} - \left(\frac{\xi Q^n}{q_c^n + Q^n} + d_E\right) E \tag{4}$$

$$\frac{dQ}{dt} = \kappa\left(\frac{I}{\phi_2 + I}\right) - d_q Q \tag{5}$$

$$A_1 = \frac{A_1^{dose}}{Vol_1} \sum_{i=1}^{3} e^{-\eta_1\left(t-\left(\tau_i+\omega_1\right)\right)} H\left(t - \left(\tau_i + \omega_1\right)\right) \tag{6}$$

$$A_2 = \frac{A_2^{dose}}{Vol_2} \sum_{i=1}^{3} e^{-\eta_2\left(t-\left(\tau_i+\omega_2\right)\right)} H\left(t - \left(\tau_i + \omega_2\right)\right) \tag{7}$$

$$A = \frac{k_1 A_1 + k_2 A_2}{K + A_1 + A_2} \tag{8}$$

Here, uninfected target CD4$^+$ T cells, T, are produced at the rate λ_T, die at the per capita rate d_T, and are infected by virions, V, with the second order rate constant β, yielding productively-infected cells, I. Cells I die at the per capita rate d_I due to viral cytopathicity and

are killed by effector CTLs, E, with the second order rate constant m. Cells I produce free virions at the rate p per cell. The virions are cleared in the absence of administered bNAbs with the rate constant c. Administered bNAbs are assumed to induce a net enhancement of the viral clearance rate by a time-dependent amount, A, which is a saturable function of the instantaneous serum concentration of the two bNAbs, 3BNC117 (A_1) and 10-1074 (A_2). The functional form mimics the 2D Hill equation derived recently to describe the effect of drug combinations (50). The net enhancement of viral clearance combines the direct effect on viral clearance by bNAbs (22) as well as the reduction in infectivity, β, due to viral neutralization by the bNAbs (51). (Because viral production and clearance are rapid compared to other processes (52), the pseudo-steady state approximation applied to Eq. (3) yields $V \approx pI/(c+A)$, which when substituted into Eqs. (1) and (2) amounts to a reduction in β by the factor $(c+A)/c$. Conversely, a reduction in β can be subsumed into an effect on c.) Administered bNAbs also bind to virions and increase antigen uptake by the rate fAV, where f depicts the effect of the bNAbs on antigen uptake relative to viral clearance. The total serum antigen available for presentation to CTLs, $I + fAV$, stimulates naïve $CD8^+$ T cells (19, 53), assumed not to be limiting, into SHIV-specific CTLs, E, with the maximal rate, ρ, and the half-maximal antigen-sensitivity parameter, ϕ_1. The saturation of the stimulation with increasing levels of total serum antigen is reflective of limitations in cellular interactions processes, such as the time to find interacting partners and the duration of each interaction (54-56). Saturating forms are argued to be more realistic than mass-action forms (55) and follow from kinetic considerations of these interactions under the total quasi-steady state approximation (56). CTLs proliferate (57) with the rate constant k_E, and suffer exhaustion (19, 58) at the maximal rate ξ, with the half-maximal parameter q_c and Hill coefficient n. The level of exhaustion, Q, increases with antigen level at the maximal rate κ and with the half-maximal parameter ϕ_2. Exhaustion is reversed with the rate constant d_q. CTLs are lost at the per capita rate d_E. We note that E is a measure of the effective CTL pool, factoring in the overall level of exhaustion, Q. E is thus not to be viewed as a CTL count. Similarly, Q is not a measure of the pool of exhausted cells. Our model of CTL stimulation and exhaustion mimics an earlier study (19). An alternative model, developed to describe post-ART control of HIV (18), also shows bistability but could not fit the present data with bNAb therapy (Figure S8 and Table S7). Similarly, variants of our model without the Hill coefficient, i.e., n=1 (18) (Figure S9, Tables

S8), with a Hill coefficient of n=3 (19) (Figure S10, Tables S9), or without an explicit CTL response (Figure S11 and Table S10) could not fit the data.

To mimic the dosing protocol in Nishimura *et al.* (10), we let the serum concentration levels of the bNAbs, A_1 and A_2, rise by the extent $\frac{A_1^{dose}}{Vol_1}$ and $\frac{A_2^{dose}}{Vol_2}$, immediately upon the administration of a bNAb dose, and decline exponentially with the rate constants η_1 and η_2, respectively. Here, A_1^{dose} and A_2^{dose} correspond to the dosages of the two bnAbs and Vol_1 and Vol_2 correspond to the bNAb-specific volumes of distribution. The three doses were administered on days $\tau_1 = 3$, $\tau_2 = 10$, and $\tau_3 = 17$, respectively. Additionally, we allowed a delay in bNAb action, ω_1 and ω_2, following each dose, to account for any pharmacological effects within individual macaques. The Heaviside function, $H\left(t < \left(\tau_i + \omega_j\right)\right) = 0$ and $H\left(t > \left(\tau_i + \omega_j\right)\right) = 1$, accounts for bNAb dynamics based on these dosing times. To compare the influence of bNAbs with that of ART, we assumed that ART reduces β by a factor $1-\epsilon$, where ϵ is the efficacy of the drug combination (18).

Long after bNAbs were cleared from circulation, Nishimura *et al.* (10) administered anti-CD8α antibodies to some macaques, which resulted in the depletion of $CD8^+$ T, NK, NKT, and $\gamma\delta$ T cells. Nishimura *et al.* (10) also administered anti-CD8β antibodies to some macaques, which only depleted $CD8^+$ T cells. To describe the resulting changes in viremia, we assumed that the depleting effects of anti-CD8α and anti-CD8β antibodies started at time points θ_α and θ_β, respectively, at which points we reduced the CTL populations by fractions ζ_α and ζ_β. Further, we assumed that anti-CD8α antibodies neutralized all host effector functions, which we modelled by setting $m = 0$ for a duration θ_m representing the residence time of the depleting antibodies.

The procedures for solving the above model equations, parameter estimation, and data fitting have been described in Text S1. All the data employed for fitting was obtained by digitizing the data published in Nishimura *et al.* (10) using the software Engauge digitizer.

Acknowledgements

We thank Alan Perelson, Rustom Antia, and Pranesh Padmanabhan for comments and Fabian Cardozo-Ojeda for help with data analysis.

Author Contributions

RD and NMD conceptualized the study. RD and RR constructed the model, estimated parameters from fits to data, and performed analyses. All authors jointly wrote the manuscript.

Conflict of Interest

The authors declare that the research was conducted in the absence of any commercial or financial relationships that could be construed as a potential conflict of interest.

Funding

This work was supported by the Wellcome Trust/DBT India Alliance Senior Fellowship IA/S/14/1/501307 (NMD).

References

1. Archin NM, Sung JM, Garrido C, Soriano-Sarabia N, & Margolis DM (2014) Eradicating HIV-1 infection: seeking to clear a persistent pathogen. *Nat Rev Microbiol* 12:750-764.

2. Whitney JB, *et al.* (2014) Rapid seeding of the viral reservoir prior to SIV viraemia in rhesus monkeys. *Nature* 512:74-77.

3. Ho YC, *et al.* (2013) Replication-competent noninduced proviruses in the latent reservoir increase barrier to HIV-1 cure. *Cell* 155:540-551.

4. Finzi D, *et al.* (1999) Latent infection of CD4+ T cells provides a mechanism for lifelong persistence of HIV-1, even in patients on effective combination therapy. *Nat Med* 5:512-517.

5. Siliciano JD, *et al.* (2003) Long-term follow-up studies confirm the stability of the latent reservoir for HIV-1 in resting CD4+ T cells. *Nat Med* 9:727-728.

6. Joos B, *et al.* (2008) HIV rebounds from latently infected cells, rather than from continuing low-level replication. *Proc Natl Acad Sci U S A* 105:16725-16730.

7. Davenport MP, *et al.* (2019) Functional cure of HIV: the scale of the challenge. *Nat Rev Immunol* 19:45-54.

8. Saez-Cirion A, *et al.* (2013) Post-treatment HIV-1 controllers with a long-term virological remission after the interruption of early initiated antiretroviral therapy ANRS VISCONTI Study. *PLoS Pathog* 9:e1003211.

9. Cockerham LR, Hatano H, & Deeks SG (2016) Post-treatment controllers: role in HIV "cure" research. *Curr HIV/AIDS Rep* 13:1-9.

10. Nishimura Y, *et al.* (2017) Early antibody therapy can induce long-lasting immunity to SHIV. *Nature* 543:559-563.

11. Bolton DL, *et al.* (2016) Human immunodeficiency virus type 1 monoclonal antibodies suppress acute simian-human immunodeficiency virus viremia and limit seeding of cell-associated viral reservoirs. *J Virol* 90:1321-1332.

12. Borducchi EN, *et al.* (2016) Ad26/MVA therapeutic vaccination with TLR7 stimulation in SIV-infected rhesus monkeys. *Nature* 540:284-287.

13. Lim SY, *et al.* (2018) TLR7 agonists induce transient viremia and reduce the viral reservoir in SIV-infected rhesus macaques on antiretroviral therapy. *Sci Transl Med* 10.

14. Borducchi EN, *et al.* (2018) Antibody and TLR7 agonist delay viral rebound in SHIV-infected monkeys. *Nature* 563:360-364.

15. Caskey M, Klein F, & Nussenzweig MC (2019) Broadly neutralizing anti-HIV-1 monoclonal antibodies in the clinic. *Nat Med* 25:547-553.

16. Bar-On Y, *et al.* (2018) Safety and antiviral activity of combination HIV-1 broadly neutralizing antibodies in viremic individuals. *Nat Med* 24:1701-1707.

17. Mendoza P, *et al.* (2018) Combination therapy with anti-HIV-1 antibodies maintains viral suppression. *Nature* 561:479-484.

18. Conway JM & Perelson AS (2015) Post-treatment control of HIV infection. *Proc Natl Acad Sci U S A* 112:5467-5472.

19. Johnson PLF, *et al.* (2011) Vaccination alters the balance between protective immunity, exhaustion, escape, and death in chronic infections. *J Virol* 85:5565-5570.

20. Baral S, Antia R, & Dixit NM (2019) A dynamical motif comprising the interactions between antigens and CD8 T cells may underlie the outcomes of viral infections. *Proc Natl Acad Sci U S A* 116:17393-17398.

21. Nishimura Y & Martin MA (2017) Of mice, macaques, and men: broadly neutralizing antibody immunotherapy for HIV-1. *Cell Host Microbe* 22:207-216.

22. Igarashi T, *et al.* (1999) Human immunodeficiency virus type 1 neutralizing antibodies accelerate clearance of cell-free virions from blood plasma. *Nat Med* 5:211-216.

23. Liu J, *et al.* (2016) Antibody-mediated protection against SHIV challenge includes systemic clearance of distal virus. *Science* 353:1045-1049.

24. Lu CL, *et al.* (2016) Enhanced clearance of HIV-1-infected cells by broadly neutralizing antibodies against HIV-1 *in vivo*. *Science* 352:1001-1004.

25. Brady LJ (2005) Antibody-mediated immunomodulation: a strategy to improve host responses against microbial antigens. *Infect Immun* 73:671-678.

26. Lu LL, Suscovich TJ, Fortune SM, & Alter G (2018) Beyond binding: antibody effector functions in infectious diseases. *Nat Rev Immunol* 18:46-61.

27. Schuurhuis DH, *et al.* (2002) Antigen-antibody immune complexes empower dendritic cells to efficiently prime specific CD8+ CTL responses in vivo. *J Immunol* 168:2240-2246.

28. Villinger F, *et al.* (2003) Evidence for antibody-mediated enhancement of simian immunodeficiency virus (SIV) Gag antigen processing and cross presentation in SIV-infected rhesus macaques. *J Virol* 77:10-24.

29. Goonetilleke N, *et al.* (2009) The first T cell response to transmitted/founder virus contributes to the control of acute viremia in HIV-1 infection. *J Exp Med* 206:1253-1272.

30. Gautam R, *et al.* (2012) Pathogenicity and mucosal transmissibility of the R5-tropic simian/human immunodeficiency virus SHIV(AD8) in rhesus macaques: implications for use in vaccine studies. *J Virol* 86:8516-8526.

31. Shingai M, *et al.* (2013) Antibody-mediated immunotherapy of macaques chronically infected with SHIV suppresses viraemia. *Nature* 503:277-280.

32. Gautam R, *et al.* (2018) A single injection of crystallizable fragment domain-modified antibodies elicits durable protection from SHIV infection. *Nat Med* 24:610-616.

33. Im SJ, *et al.* (2016) Defining CD8+ T cells that provide the proliferative burst after PD-1 therapy. *Nature* 537:417.

34. Wykes MN & Lewin SR (2018) Immune checkpoint blockade in infectious diseases. *Nat Rev Immunol* 18:91-104.

35. Mutua G, *et al.* (2016) Broad HIV-1 inhibition in vitro by vaccine-elicited CD8(+) T cells in African adults. *Mol Ther Methods Clin Dev* 3:16061.

36. Garcia F, *et al.* (2013) A dendritic cell-based vaccine elicits T cell responses associated with control of HIV-1 replication. *Sci Transl Med* 5:166ra162.

37. Murakoshi H, *et al.* (2018) CD8(+) T cells specific for conserved, cross-reactive Gag epitopes with strong ability to suppress HIV-1 replication. *Retrovirology* 15:46.

38. Pan E, *et al.* (2018) Immune protection of SIV challenge by PD-1 blockade during vaccination in rhesus monkeys. *Front Immunol* 9:2415.

39. Mothe B & Brander C (2018) HIV T-cell vaccines. *HIV vaccines and cure : The path towards finding an effective cure and vaccine*, eds Zhang L & Lewin SR (Springer Singapore, Singapore), pp 31-51.

40. Kohli A, *et al.* (2015) Virological response after 6 week triple-drug regimens for hepatitis C: a proof-of-concept phase 2A cohort study. *The Lancet* 385:1107-1113.

41. Baral S, Roy R, & Dixit NM (2018) Modeling how reversal of immune exhaustion elicits cure of chronic hepatitis C after the end of treatment with direct-acting antiviral agents. *Immunol Cell Biol*.

42. Goyal A, *et al.* (2017) Modeling HCV cure after an ultra-short duration of therapy with direct acting agents. *Antivir Res* 144:281-285.

43. Nguyen THT, *et al.* (2017) The paradox of highly effective sofosbuvir-based combination therapy despite slow viral decline: can we still rely on viral kinetics? *Sci Rep* 7:10233.

44. DiLillo DJ & Ravetch JV (2015) Differential Fc-receptor engagement drives an anti-tumor vaccinal effect. *Cell* 161:1035-1045.

45. Hashimoto M, *et al.* (2018) CD8 T cell exhaustion in chronic infection and cancer: opportunities for interventions. *Ann Rev Med* 69:301-318.

46. Schoofs T, *et al.* (2016) HIV-1 therapy with monoclonal antibody 3BNC117 elicits host immune responses against HIV-1. *Science* 352:997-1001.

47. Doitsh G, *et al.* (2014) Cell death by pyroptosis drives CD4 T-cell depletion in HIV-1 infection. *Nature* 505:509-514.

48. Wang S, Hottz P, Schechter M, & Rong L (2015) Modeling the slow CD4+ T cell decline in HIV-infected individuals. *PLoS Comput Biol* 11:e1004665.

49. Shankarappa R, *et al.* (1999) Consistent viral evolutionary changes associated with the progression of human immunodeficiency virus type 1 infection. *J Virol* 73:10489-10502.

50. Meyer CT, *et al.* (2019) Quantifying drug combination synergy along potency and efficacy axes. *Cell Syst* 8:97-108 e116.

51. Klein F, *et al.* (2013) Antibodies in HIV-1 vaccine development and therapy. *Science* 341:1199-1204.

52. Nowak M & May RM (2000) *Virus dynamics: mathematical principles of immunology and virology* (Oxford University Press, UK).

53. Bevan MJ (2004) Helping the CD8+ T-cell response. *Nat Rev Immunol* 4:595-602.

54. Nagaraja P, Alexander HK, Bonhoeffer S, & Dixit NM (2016) Influence of recombination on acquisition and reversion of immune escape and compensatory mutations in HIV-1. *Epidemics* 14:11-25.

55. Wodarz D (2014) Modeling T cell responses to antigenic challenge. *J Pharmacokinet Pharmacodyn* 41:415-429.

56. Borghans JA, de Boer RJ, & Segel LA (1996) Extending the quasi-steady state approximation by changing variables. *Bull Math Biol* 58:43-63.

57. Mempel TR, Henrickson SE, & Von Andrian UH (2004) T-cell priming by dendritic cells in lymph nodes occurs in three distinct phases. *Nature* 427:154-159.

58. Wherry EJ & Kurachi M (2015) Molecular and cellular insights into T cell exhaustion. *Nat Rev Immunol* 15:486-499.

Figures

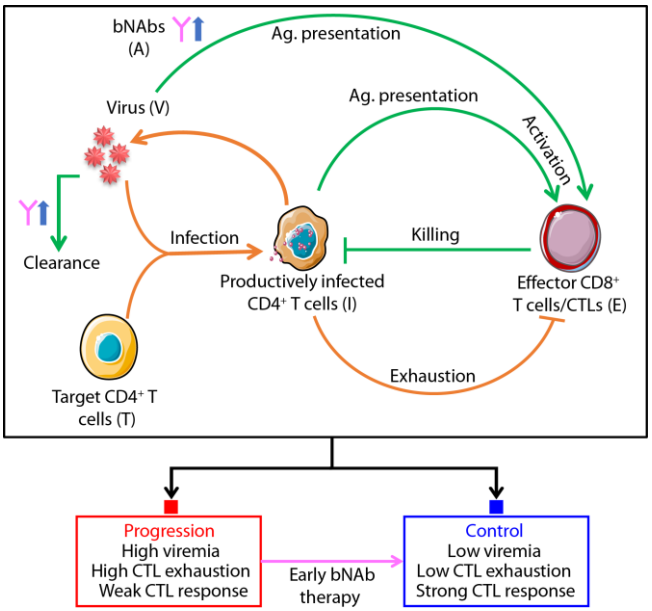

Figure 1: Schematic of the mathematical model of SHIV dynamics with bNAb therapy. Orange and green arrows indicate processes involved in the growth and control of infection, respectively. The steps influenced by bNAbs are shown with thick blue arrows. Corresponding model equations are described in Methods. Steady state analysis of the model indicates two outcomes of the infection: chronic infection with high viremia that marks progressive disease (red filled square), typically realized in the absence of treatment, and viremic control (blue filled square), a switch to which is orchestrated by early bNAb therapy.

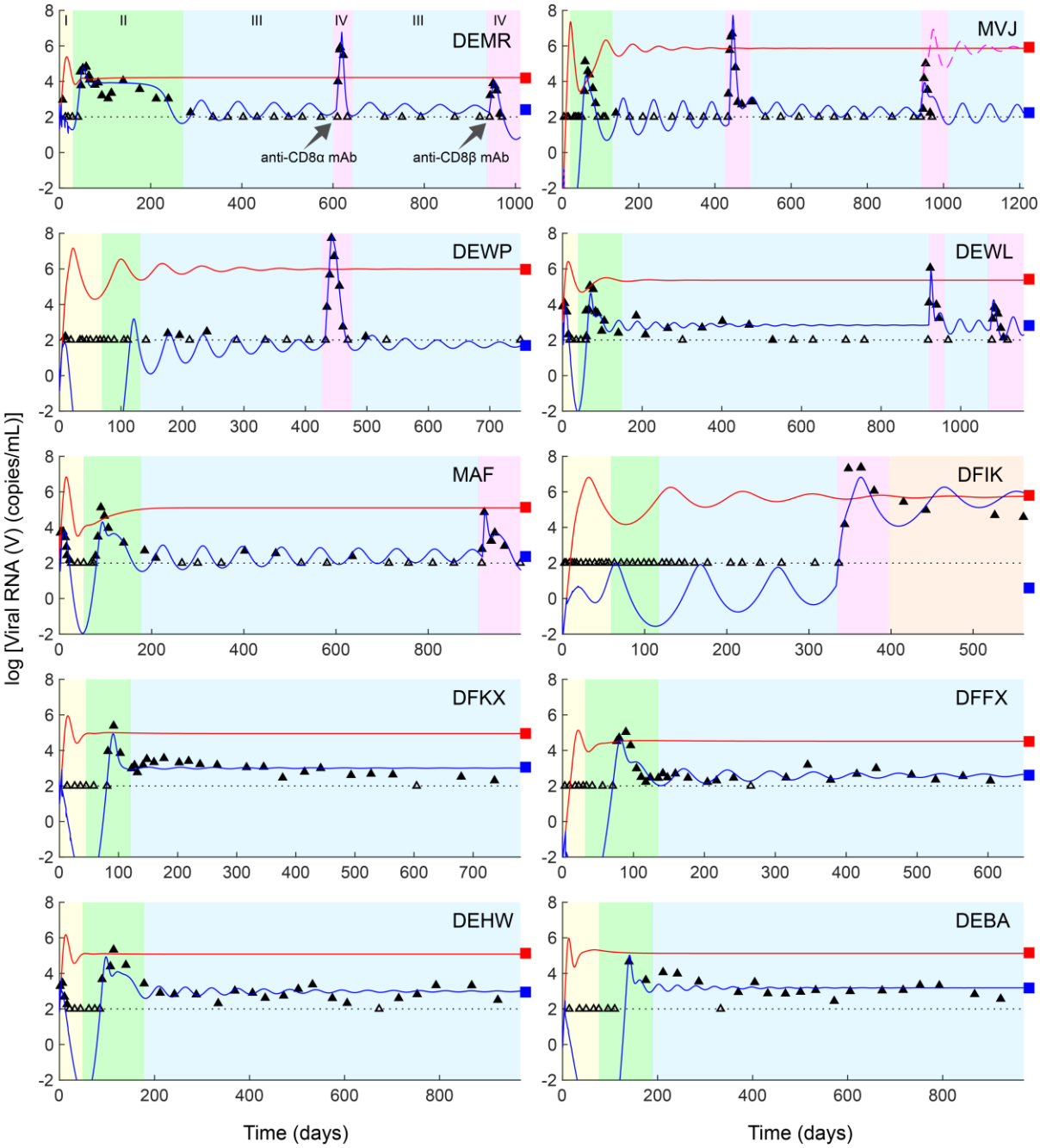

Figure 2: Model fits viral dynamics in responder macaques. Model fits (blue lines) to viral load data (10) (symbols) from the 10 controller macaques (10), shown in individual panels. Empty symbols mark measurements showing undetectable viremia and filled symbols above detection. The latter were censored for fitting. Black dashed lines in all panels indicate the viral load detection limit (100 RNA copies/mL). The corresponding bNAb concentration dynamics are in Figure S1. In all panels, phase I (yellow) marks the duration when bNAbs are present in circulation, phase II (green) the viremic resurgence post the clearance of bNAbs, phase III (blue) the ensuing viremic control, and, where relevant, phase IV (pink), in two parts, the disruption of this control using anti-CD8α and anti-CD8β Abs, respectively. For the macaque MVJ, we demonstrate the loss of viral control that occurs when CTL depletion levels are increased (magenta line), as is observed with the macaque DFIK. The data used for the fitting is available in Database S1. In all cases, predictions without bNAb therapy are included for comparison (red lines). Parameter values used are in Tables S1 and S3. Macaques DEWP, MVJ, DFFX, DFKX, and DFIK were inoculated intrarectally and DEWL and MAF intravenously with 1000 $TCID_{50}$ (50% tissue culture infective dose) of $SHIV_{AD8\text{-}EO}$ virus. DEMR, DEBA, and DEHW received 100 $TCID_{50}$ intravenously.

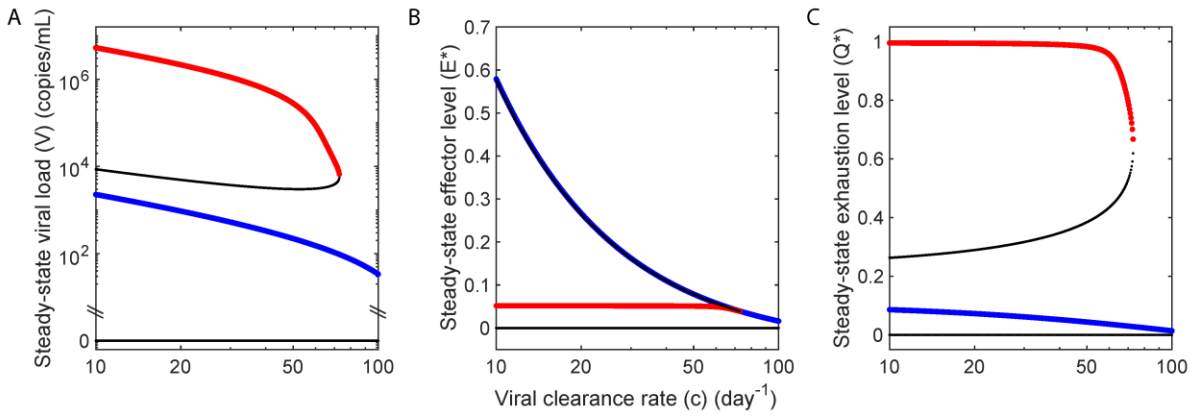

Figure 3: Bifurcation diagrams indicating the two distinct outcomes of progressive disease and viremic control. Model calculations of the steady state (**a**) viral load, (**b**) normalized effector level ($E^*=Ed_E/\rho$) , and (**c**) normalized level of exhaustion ($Q^*=Qd_q/\kappa$), obtained by varying the viral clearance rate. The stable states of progressive disease and viremic control are shown in red and blue, respectively. Thin black lines represent unstable steady states. In (b), the intermediate unstable state lies close to the state of viremic control. The steady states are separated by other state variables, including the level of exhaustion, evident in (c). Parameter values used are in Tables S1 and S2. Bifurcation diagrams for other parameters are shown in Figure S3.

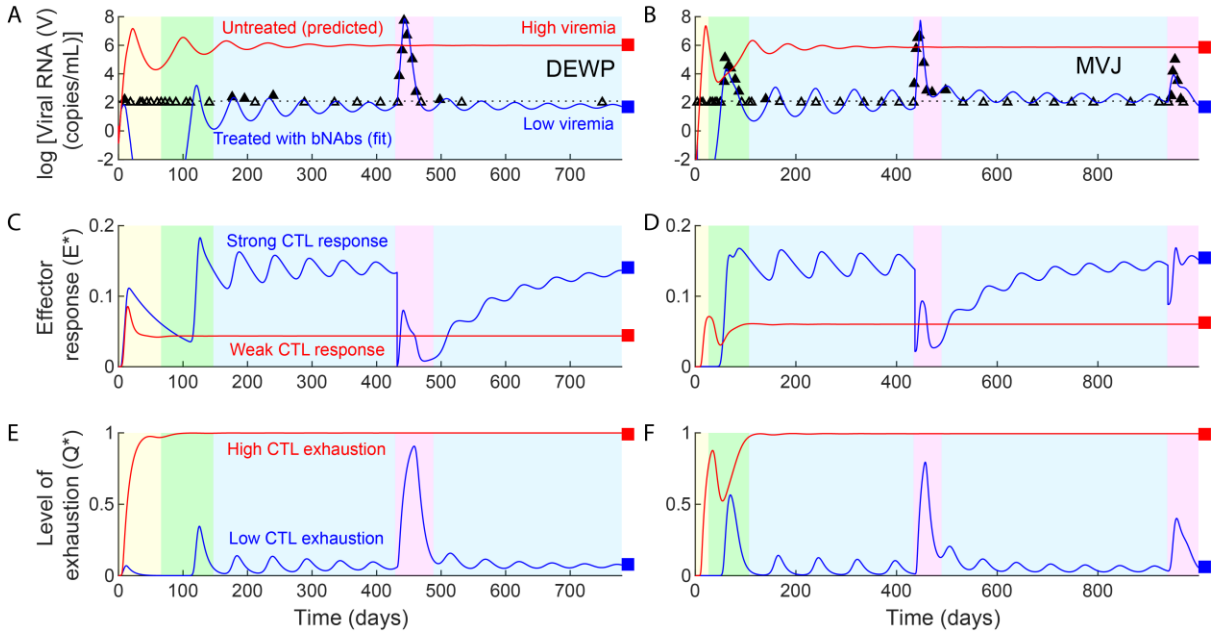

Figure 4: Early bNAb therapy induces a switch to viremic control. (**a,b**) Model fits (blue lines) to viral load data (10) (symbols) from the responder macaques DEWP and MVJ. (The parameter values used are in Tables S1 and S3). The corresponding dynamics of (**c,d**) the CTL response and (**e,f**) the level of CTL exhaustion. The phases are color coded as in Figure 2. Red lines in all panels indicate model predictions with the same parameter values but in the absence of bNAb therapy. Our model predicts thus that bNAb therapy switches disease dynamics from reaching the high viremic, disease progressive state to the state of viremic control. Black dashed lines in (**a,b**) indicate the viral load detection limit (100 RNA copies/mL).

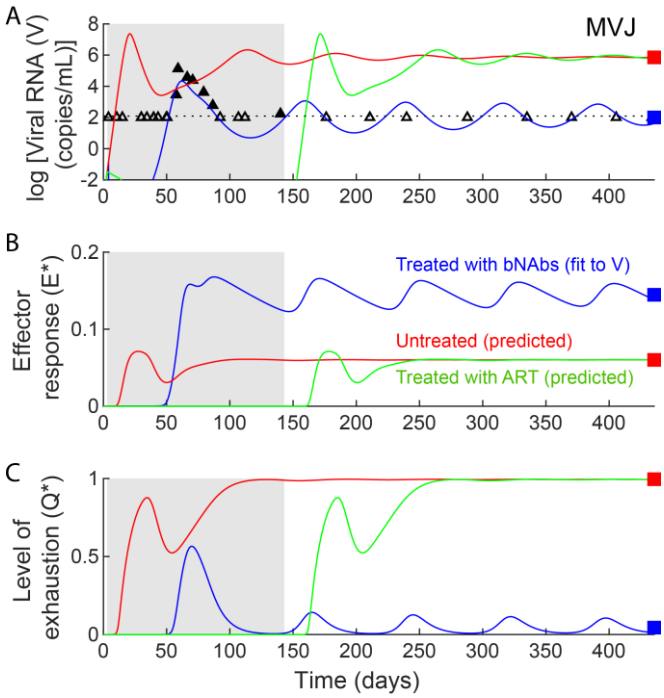

Figure 5: bNAbs succeed whereas ART fails to establish long-term viremic control. Simulated dynamics of **(a)** viral load, **(b)** CTL response, and **(c)** CTL exhaustion with ART (green lines) are shown in comparison with the corresponding dynamics without treatment (red lines) and with bNAb treatment (blue lines) using parameters that capture data for the macaque MVJ (symbols). (Parameter values used are in Tables S1 and S3.) The duration of ART is shown as a grey region. The black dashed lines in (**a**) indicates the viral load detection limit (100 RNA copies/mL).

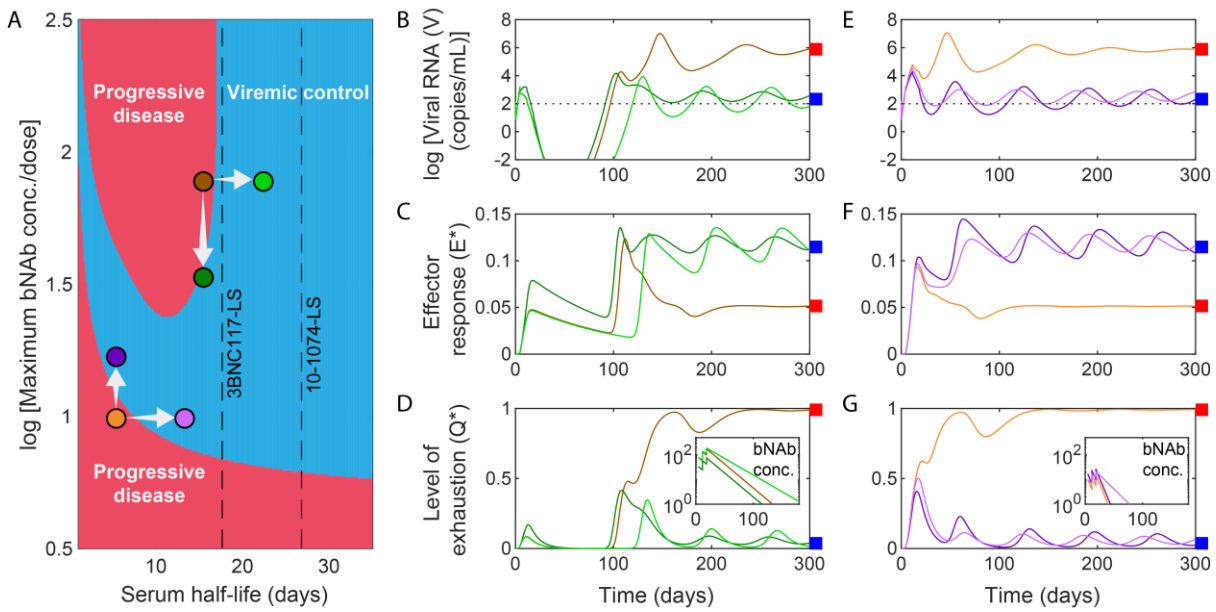

Figure 6: Strategies to optimize bNAb therapy. (**a**) Model predictions of the phase diagram showing combinations of the maximum bNAb concentration achieved with a single dose and bNAb half-life yielding viremic control (blue) or leading to progressive disease (red). Parameter values used are in Tables S1 and S2. In addition, here we considered the dynamics of latently infected cells (Text S1). (**b-d**) Representative viral dynamics showing treatment failure in the upper red region (brown lines), which can be averted with a lower bNAb dose (dark green lines) or longer half-life (light green lines). (**e-f**) Corresponding viral dynamics showing treatment failure in the lower red region (orange lines), which can be averted with a higher bNAb dose (purple lines) or longer half-life (pink lines). Insets in (**d**) and (**g**) show the time-evolution of effective bNAb levels in circulation. The corresponding conditions are indicated with similarly colored boxes in the phase diagram in (**a**). The dashed vertical lines indicate half-lives of the bNAbs estimated for the macaque MVJ (Table S1) and those for the bNAbs engineered with the LS mutations (32). Variations due to uncertainties in bNAb pharmacokinetics are shown in Figure S6.

Supplementary Material:
Early exposure to broadly neutralizing antibodies triggers a switch from progressive disease to lasting control of SHIV infection

Rajat Desikan[1†‡*], Rubesh Raja[1†] and Narendra M. Dixit[1,2*]

[1]*Department of Chemical Engineering,* [2]*Centre for Biosystems Science and Engineering, Indian Institute of Science, Bengaluru, India, 560012*
[†]*Shared first authorship.*
[‡]*Present address: Akamara Biomedicine Private Limited, Ist Floor, No. 465, Patparganj Industrial Area, Delhi, India, 110092*
[*]Corresponding authors, E-mail: rajatdesikan@gmail.com, narendra@iisc.ac.in; Tel: +91-80-2293-2768, +91-9880842145

Text S1. Supplementary methods

Solution of model equations

For ease of solution and parameter estimation, we rescaled Eqs 1-8 in the main text using the quantities in Eqs S1 and S2 and obtained an equivalent model with fewer parameters (Eqs S3-S10). bNAb concentrations, A_1 and A_2, and viral load, V, were not scaled because they were used for fitting data.

$$T^* = T\frac{d_T}{\lambda_T},\ I^* = I\frac{d_T}{\lambda_T},\ E^* = E\frac{d_E}{\rho},\ Q^* = Q\frac{d_q}{\kappa} \tag{S1}$$

$$p^* = p\frac{\lambda_T}{d_T},\ m^* = m\frac{\rho}{d_E},\ f^* = f\frac{d_T}{\lambda_T},\ \phi^* = \phi_1\frac{d_T}{\lambda_T} = \phi_2\frac{d_T}{\lambda_T},\ q_c^* = q_c\frac{d_q}{\kappa} \tag{S2}$$

$$\frac{dT^*}{dt} = d_T\left(1-T^*\right) - \beta V T^* \tag{S3}$$

$$\frac{dI^*}{dt} = \beta V T^* - \left(d_I + m^* E^*\right) I^* \tag{S4}$$

$$\frac{dV}{dt} = p^* I^* - (c+A)\,V \tag{S5}$$

$$\frac{dE^*}{dt} = \frac{\left(d_E + k_E E^*\right)\left(I^* + f^* A V\right)}{\left(\phi^* + I^* + f^* A V\right)} - \left(\frac{\xi\left(Q^*\right)^n}{\left(q_c^*\right)^n + \left(Q^*\right)^n} + d_E\right) E^* \tag{S6}$$

$$\frac{dQ^*}{dt} = d_q\left(\frac{I^*}{\phi^* + I^*} - Q^*\right) \tag{S7}$$

$$A_1 = \left(\frac{A_1^{dose}}{Vol_1}\right)\sum_{i=1}^{3} e^{-\eta_1\left(t-\left(\tau_i+\omega_1\right)\right)} H\left(t-\left(\tau_i+\omega_1\right)\right) \tag{S8}$$

$$A_2 = \left(\frac{A_2^{dose}}{Vol_2}\right)\sum_{i=1}^{3} e^{-\eta_2\left(t-\left(\tau_i+\omega_2\right)\right)} H\left(t-\left(\tau_i+\omega_2\right)\right) \tag{S9}$$

$$A = \frac{k_1 A_1 + k_2 A_2}{K + A_1 + A_2} \tag{S10}$$

The model equations were integrated using the initial conditions $T^*(0) = 1$, $I^*(0) = E^*(0) = Q^*(0) = 0$, $A_1(0) = \frac{A_1^{dose}}{Vol_1}$ and $A_2(0) = \frac{A_2^{dose}}{Vol_2}$. The initial viral load, $V(0)$, varied for individual macaques and was estimated from fits.

We also obtained steady state solutions by setting the left-hand sides of all equations to zero and solving the resulting coupled non-linear equations in Mathematica. We subsequently performed linear stability analysis, by computing the eigenvalues of the Jacobian matrix of the above dynamical system,

to assess the stability of the steady states.

Parameter estimates and data fitting

The data available from Nishimura *et al.* ([1]) for fitting this model consists of longitudinal values of the plasma SHIV viral load (V) and serum bNAb concentrations (A_1 and A_2). For this model, we performed formal identifiability analysis of the model parameters by employing the Exact Arithmetic Rank (EAR) implementation in Mathematica (IdentifiabilityAnalysis package ([2])), assuming that measurements of V, A_1 and A_2 are perfect and continuous in time. The analysis revealed that upon fixing A_1^{dose} and A_2^{dose}, whose values can be estimated from Nishimura *et al.* ([1]), all the other parameters in the model are fully identifiable from the data.

Wherever possible, we fixed model parameter values based on previously published estimates (Table S1). For instance, following Conway and Perelson ([3]), we fixed the death rate of target cells, $d_T = 0.01$ day^{-1}. We let the death rate of infected cells due to viral cytopathicity be $d_I = 0.5$ day^{-1}, which is $\sim 50\%$ of the mean overall death rate of infected cells ([4]), and lies at the lower end of the range of the overall death rate, $0.5 - 1.7$ day^{-1} for HIV-1 ([5]), with the rest attributed to effector killing. The viral clearance rate was estimated ([3,6]) to be $c = 23$ day^{-1} for HIV-1, but has been shown to be much higher ($c = 38 - 302$ day^{-1}) for SIV ([7–9]). We conservatively chose a value of $c = 38$ day^{-1}. Similarly, for an estimate of CTL expansion rate, k_E, we considered previous reports that found that 66% of CD8 T cells activated with a specific Ag proliferate with a time to cell division of 12.9 h, while the rest either die or become resting ([10]). This yielded a mean proliferation rate of ~ 1 day^{-1}. Additionally, only 73% unactivated T cells get activated ([11]), and T cell clones specific to sub-dominant epitopes could proliferate at a rate 2-fold lower than clones specific to the immunodominant epitopes ([9,10]). Here, we separated CTL activation and proliferation and chose the maximal proliferation rate conservatively as $k_E = 0.1$ day^{-1}. (Preliminary fits with k_E adjustable yielded fit values of $k_E \sim 0.1$ day^{-1}, but the model had a much higher AIC.) We set the Hill coefficient for exhaustion, $n = 4$, following studies that recognize underlying non-linearities ([3,12]) and because smaller integral values of n did not yield good fits (see below). Further, we set $\phi_1 = \phi_2 = \phi$ following earlier studies ([12]) and because fitting them as separate variables yielded best-fit values that were close, $\phi_1 \sim 2.1 \times 10^{-5}$ and $\phi_2 \sim 5.7 \times 10^{-5}$, but with a higher value of the Akaike Information Criterion (AIC) (4078 vs. 3998 assuming $\phi_1 = \phi_2$).

We divided the remaining parameters into two sets, $\vartheta = \{\beta,\ m^*,\ p^*,\ f^*,\ \phi^*,\ d_E,\ \xi,\ V(0),\ Vol_1,\ Vol_2,\ k_1,\ k_2,\ K\}$ and $\rho = \{\omega_1,\ \omega_2,\ \eta_1,\ \eta_2\}$, the former assumed to follow log-normal and the latter logit-normal distributions, respectively. To estimate these parameters, we employed a population-based fitting approach using non-linear mixed effects (NLME) models to jointly fit the log plasma viral load (both treated and untreated animals) and antibody concentrations of the ten responder macaques in Nishimura *et al.* ([1]) which do not exhibit consistent $CD4^+$ decline: DEMR, MVJ, DEWP, DEWL, MAF, DFIK, DFKX, DFFX, DEHW, and DEBA. (A supplementary excel file, *Database S1.xlsx*, containing digitized viral loads and serum concentrations of bNAbs 3BNC117 and 10-1074 with time for all bNAb-treated and untreated macaques from Nishimura *et al* ([1]) is available with this manuscript.) Briefly, the parameters for all the individual macaques were assumed to be sampled from a common population distribution, and the aim of the fitting exercise was to obtain estimates for the mean and variance of this distribution for each parameter. For each macaque i, parameters ϑ_i were estimated assuming underlying log-normal distributions of the form:

$$log\,(\vartheta_i) = log\ \mu + \psi_i \tag{S11}$$

where μ is the set of the population means and $\psi_i \sim N(0,\sigma)$ are normally distributed 'random effects' whose variances are to be estimated. Similarly, parameters ρ_i for macaque i were estimated assuming underlying logit-normal distributions of the form:

$$log\left(\frac{\rho_i - \rho_i^{min}}{\rho_i^{max} - \rho_i}\right) = log\left(\frac{\mu - \rho_i^{min}}{\rho_i^{max} - \mu}\right) + \psi_i \tag{S12}$$

where ρ_i^{min} and ρ_i^{max} are the minimum and maximum allowed values for parameters in ρ_i. The latter limits were set so that $\omega_1, \omega_2 \in [0,5]$, and $\eta_1, \eta_2 \in [0.01 - 7]$ day^{-1}, expected from the 1 week dosing interval employed. To account for measurement errors in observed viral loads and bNAb levels ($y(t)$), we defined a 'combined error' model such that $y(t)$ is normally distributed around a true value ($y^*(t)$) as described by the following equation:

$$y(t) = y^*(t) + (a + b\,y^*(t))\ \psi_y(t), \quad \psi_y \sim N(0,1) \tag{S13}$$

where a is the constant error term and b is the error term proportional to the true value, $y^*(t)$.

All fitting except CD8 depletion was performed using Monolix software version 2019R1 (`www.lixoft.eu`), where the population estimates were obtained by maximum likelihood estimation. Untreated monkeys infected with the $\text{SHIV}_{\text{AD8-EO}}$ viral strain consistently proceed towards high viremic chronic infection and immunodeficiency ([13–15]). To recapitulate this behaviour, we simultaneously solved the model without bNAbs and ensured that the set point viral load attained values greater than $10^{3.5}$ copies/mL (enforced using the 'censoring' keyword during data input in Monolix). Parameter exploration was carried out using the stochastic approximation using expectation maximization (SAEM) algorithm implemented in Monolix ([16]), and we simulated a large number of realizations $(100-200)$ to produce consistent final parameter estimates that were biologically realistic. Comparisons of some of the population parameters with independent estimates from previous studies further validated our fitting procedure. For instance, the estimated population value of p^* corresponds to a burst size of 6595 virions per infected cell (Table S2), consistent with current estimates of $\sim 10^4$ virions per cell[17] given a target cell production rate ([3]) of $\lambda_T = 10^4$ cells mL^{-1} day^{-1}. Similarly, the estimated $\beta = 10^{-8}$ virion^{-1} mL day^{-1} is also close to the previous estimate of 2.4×10^{-8} virion^{-1} mL day^{-1} ([5]). Finally, we note that the enhanced clearance rate of virions, $c+A$, has a maximum of ~ 145 day^{-1}, which is ~ 3.8-fold above the natural clearance rate, $c = 38$ day^{-1}, consistent with the $3-4$ fold increase in clearance rate due to bNAbs observed in other studies ([7]).

For capturing CD8$^+$ T cell depletion experiments, since explicit dynamics of the anti-CD8 antibodies were not available from Nishimura *et al.* ([1]), simultaneous fitting with Monolix consistently yielded poor fits to viral load data, especially in phase II (green region in Figure 2), often with unrealistic parameter estimates. Therefore, we first obtained parameters for each monkey from the population fits without CD8 depletion, and subsequently, using these parameters, we fit viral loads upon CD8$^+$ T cell depletion to individual monkey data. Briefly, Nishimura *et al.* ([1]) administered anti-CD8α antibodies to 6 macaques (MVJ, DEMR, DEWL, DEWP, MAF and DFIK) that resulted in depletion of CD8$^+$ T, NK, NKT, and $\gamma\delta$ T cells. All macaques exhibited a sharp increase in viremia, followed by reassertion of control in 5 macaques, and loss of control in one macaque (DFIK). Nishimura *et al.* ([1]) also administered anti-CD8β antibodies to 3 macaques (MVJ, DEMR and DEWL) that only depleted CD8$^+$ T cells,

resulting in a smaller increase in viremia compared to the administration of anti-CD8α antibodies. We captured these observations through model predictions for macaques MVJ, DEMR, DEWL, and MAF. We assumed that the depleting effects of anti-CD8α and anti-CD8β antibodies started at time points θ_α and θ_β, respectively, at which points we reduced the effector populations by fractions ζ_α and ζ_β. Further, we assumed that anti-CD8α antibodies neutralized all host effector functions, which we modeled by setting $m = 0$ for a duration θ_m representing the residence time of the depleting antibodies. We fit θ_α, θ_β, θ_m, ζ_α, and ζ_β to viral load data following the administration of depleting antibodies from all macaques (best-fits in phase IV of Figure 2). Fits were obtained using the 'multistart' and 'lsqcurvefit' tools along with the ode15s solver in Matlab (`in.mathworks.com`).

Phase diagram of treatment outcomes

For obtaining the bNAb dose/half-life phase diagrams (Figure 6 and Figure S7), we solved the model assuming the administration of a single bNAb. (Visualizing the phase behaviour with multiple bNAbs is difficult; besides, a single bNAb plays effectively the same role as multiple bNAbs combined, in the absence of resistance.) Further, at high doses of bNAbs, the model can behave like with ART and drive V to low values, where the contribution from latently infected cells can become significant. We therefore also incorporated the dynamics of latently infected cells, L, similar to Conway and Perelson ([3]). The resulting dynamics of I, L, and the combined bNAb efficacy, A, were described as follows:

$$I^* = I\frac{d_T}{\lambda_T},\ L^* = L\frac{d_T}{\lambda_T} \tag{S14}$$

$$\frac{dI^*}{dt} = (1-f_L)\,\beta V T^* + aL^* - (d_I + m^* E^*)\,I^* \tag{S15}$$

$$\frac{dL^*}{dt} = f_L \beta V T^* + (\psi - a - d_L)\,L^* \tag{S16}$$

$$A_m = \left(\frac{A^{dose}}{Vol}\right)\sum_{i=1}^{3} e^{-\eta_m(t-(\tau_i+\omega_m))}\,H\left(t-(\tau_i+\omega_m)\right) \tag{S17}$$

$$A = \frac{k_m A_m}{K + A_m} \tag{S18}$$

where $k_m = mean(k_1, k_2)$, $\eta_m = mean(\eta_1, \eta_2)$, and $\omega_m = mean(\omega_1, \omega_2)$, and f_L is the fraction of infections that yields cells L. Cells L proliferate, get activated, and die at the per capita rates ψ, a, and d_L,

respectively. These parameters were fixed to $f_L = 10^{-6}$, $\psi = 0.0045$ day^{-1}, $a = 0.001$ day^{-1}, and $d_L = 0.004$ day^{-1} following Conway and Perelson ([3]). All other parameters were fixed to our population estimates (Table S2). We plot the phase diagram using the maximum bNAb concentration achieved following a single dose $\left(\frac{A^{dose}}{Vol}\right)$, which is also the increase in the bNAb concentration per dose (see Eq S17), and the bNAb half-life $\left(\frac{ln(2)}{\eta_m}\right)$ as independent variables in Figure 6 and Figure S7.

Model variants

Many model variants were tested for their ability to accurately capture the data with fewer parameters.

CTL exhaustion. We also test a simpler model of exhaustion, previously reported by Conway and Perelson ([3]), where the loss of effector cells due to exhaustion is a saturating function of the antigen density. The scaled model equations are:

$$T^* = T\frac{d_T}{\lambda_T},\ I^* = I\frac{d_T}{\lambda_T},\ L^* = L\frac{d_T}{\lambda_T},\ E^* = E\frac{d_E}{\rho} \tag{S19}$$

$$p^* = p\frac{\lambda_T}{d_T},\ m^* = m\frac{\rho}{d_E},\ f^* = f\frac{d_T}{\lambda_T},\ \phi_1^* = \phi_1\frac{d_T}{\lambda_T},\ \phi_2^* = \phi_2\frac{d_T}{\lambda_T} \tag{S20}$$

$$\frac{dT^*}{dt} = d_T\left(1-T^*\right) - \beta V T^* \tag{S21}$$

$$\frac{dI^*}{dt} = (1-f_L)\beta V T^* + aL^* - (d_I + m^* E^*) I^* \tag{S22}$$

$$\frac{dL^*}{dt} = f_L \beta V T^* + (\psi - a - d_L) L^* \tag{S23}$$

$$\frac{dV}{dt} = p^* I^* - (c + A) V \tag{S24}$$

$$\frac{dE^*}{dt} = d_E + \frac{k_E E^* \left(I^* + f^* A V\right)}{\left(\phi_1^* + I^* + f^* A V\right)} - \left(\frac{\xi I^*}{\phi_2^* + I^*} + d_E\right) E^* \tag{S25}$$

bNAb pharmacodynamics (A_1 and A_2) remain the same as Eqs. S9 and S10. ϕ_1 and ϕ_2 are the CTL activation and exhaustion thresholds, respectively. In this model, a fraction (f_L) of uninfected CD4$^+$ infections yield latently-infected cells ([18]), L, and the rest, productively-infected cells, I. Cells L proliferate, get activated, and die at the per capita rates ψ, a, and d_L, respectively. We again followed the population-based fitting strategy above. The model failed to capture the viral load patterns observed within the 200 stochastic realizations employed (Figure S8).

Hill coefficient. The Hill coefficient for exhaustion, n, which dictates the sharpness of the exhaustion switch, cannot be accurately estimated from the data. While we use $n = 4$ (Eq. S6), previous studies have used values of 1 and 3 ([3,12]). Therefore, by employing the same population-based fitting procedure detailed above and with $100-200$ realizations per model, we fit V, A_1 and A_2 to model variants with Hill coefficients $n = 1$ and $n = 3$. While the model with $n = 1$ failed to capture the viral loads (Figure S9), with $n = 3$, viral load patterns upon early bNAb therapy, but not CTL depletion (Figure S10), were captured. Specifically, upon CTL depletion with anti-CD8α and anti-CD8β antibodies for monkeys DEWP and MVJ, respectively, while *in vivo* experimental measurements by Nishimura *et al.,* ([1]) showed re-establishment of control, fits exhibit loss of control and attainment of the high viremic steady state.

Absence of CTLs. Lastly, we checked whether a basic viral dynamics model, with the latent pool but without CTLs could capture the macaque viral load data. The scaled model equations are:

$$T^* = T\frac{d_T}{\lambda_T},\ I^* = I\frac{d_T}{\lambda_T},\ L^* = L\frac{d_T}{\lambda_T},\ p^* = p\frac{\lambda_T}{d_T} \tag{S26}$$

$$\frac{dT^*}{dt} = d_T\,(1-T^*) - \beta V T^* \tag{S27}$$

$$\frac{dI^*}{dt} = (1-f_L)\,\beta V T^* + aL^* - (d_I + m^* E^*)\,I^* \tag{S28}$$

$$\frac{dL^*}{dt} = f_L \beta V T^* + (\psi - a - d_L)\,L^* \tag{S29}$$

$$\frac{dV}{dt} = p^* I^* - (c+A)\,V \tag{S30}$$

where bNAb pharmacodynamics (A_1 and A_2) remain as before (Eqs. S9 and S10). Again, the model could not capture the *in vivo* temporal viremic patterns (Figure S11), reaffirming the role of the CTL response in establishing robust viremic control.

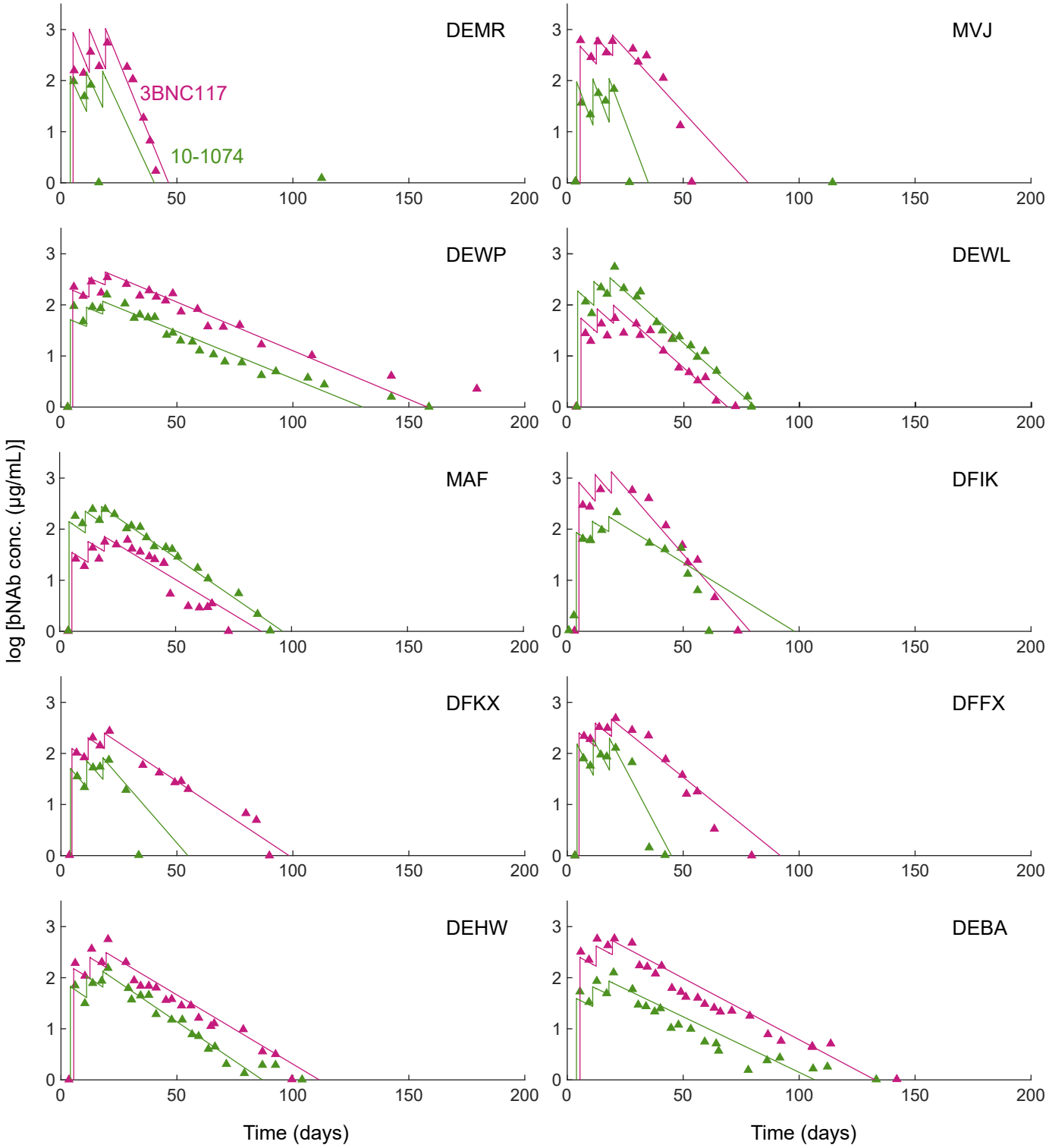

Fig. S1 bNAb pharmacokinetics in responders. Fits of model predictions (lines) to data from individual macaques (symbols) of bNAb plasma concentrations for the ten responders in Nishimura *et al.* ([1]) obtained by simultaneously fitting our model (Eqs. S3-S10) to V, A_1 and A_2 across all macaques. See Text S1 for the fitting procedure. The resulting parameter estimates are in Table S3. The bNAb serum half-lives averaged across all macaques are 9.2 days (range $2.7-15.8$ days) for 3BNC117, and 8.4 days (range $2.5-16.3$ days) for 10-1074.

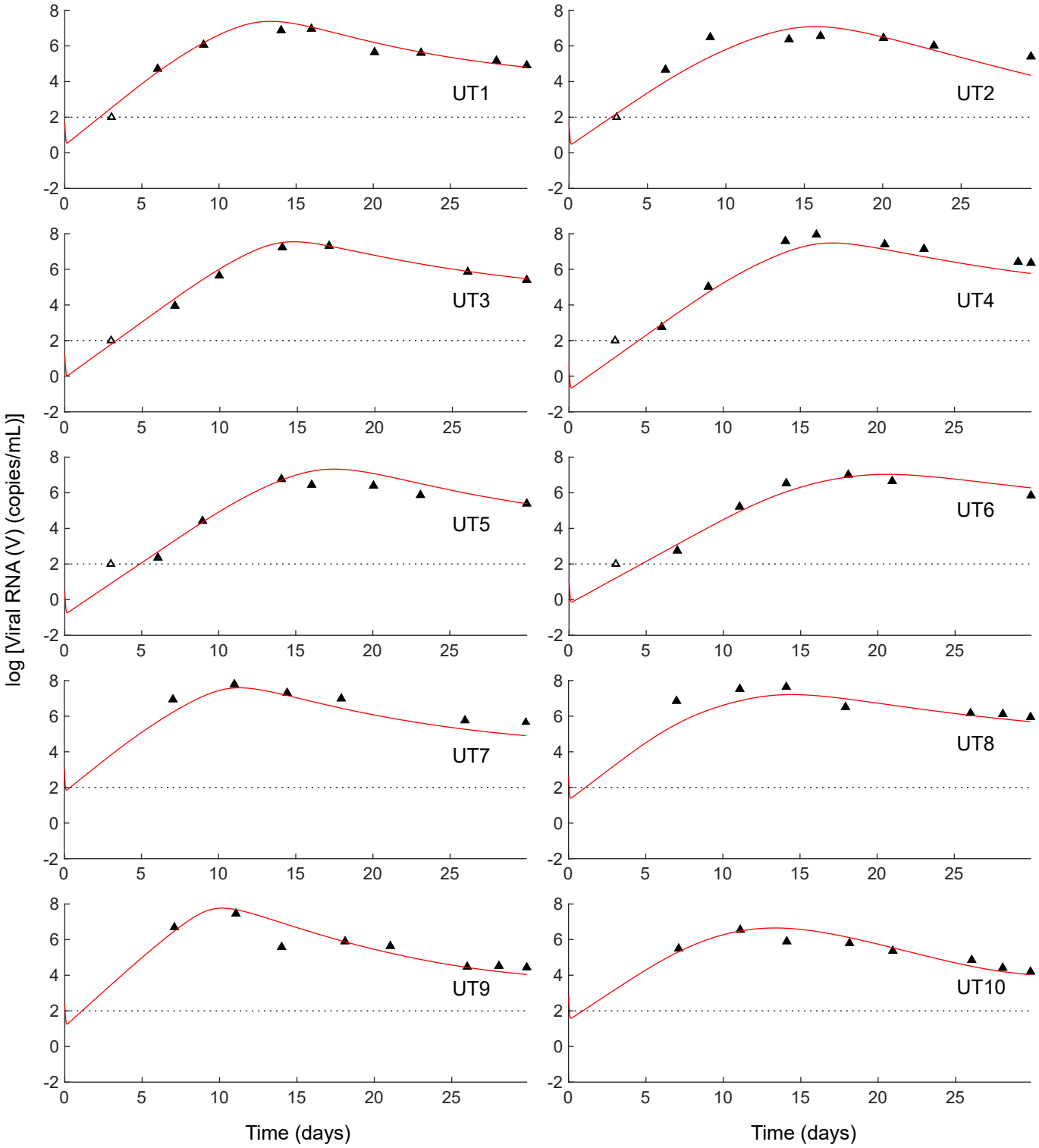

Fig. S2 Untreated macaques. Fits (red lines) to the acute phase viral loads of the ten untreated macaques in Nishimura *et al.,* ([1]) obtained by simultaneously fitting our model (Eqs. S3-S10) to V, A_1 and A_2 across all macaques. See Text S1 for the fitting procedure. The best-fit parameter estimates are in Table S4.

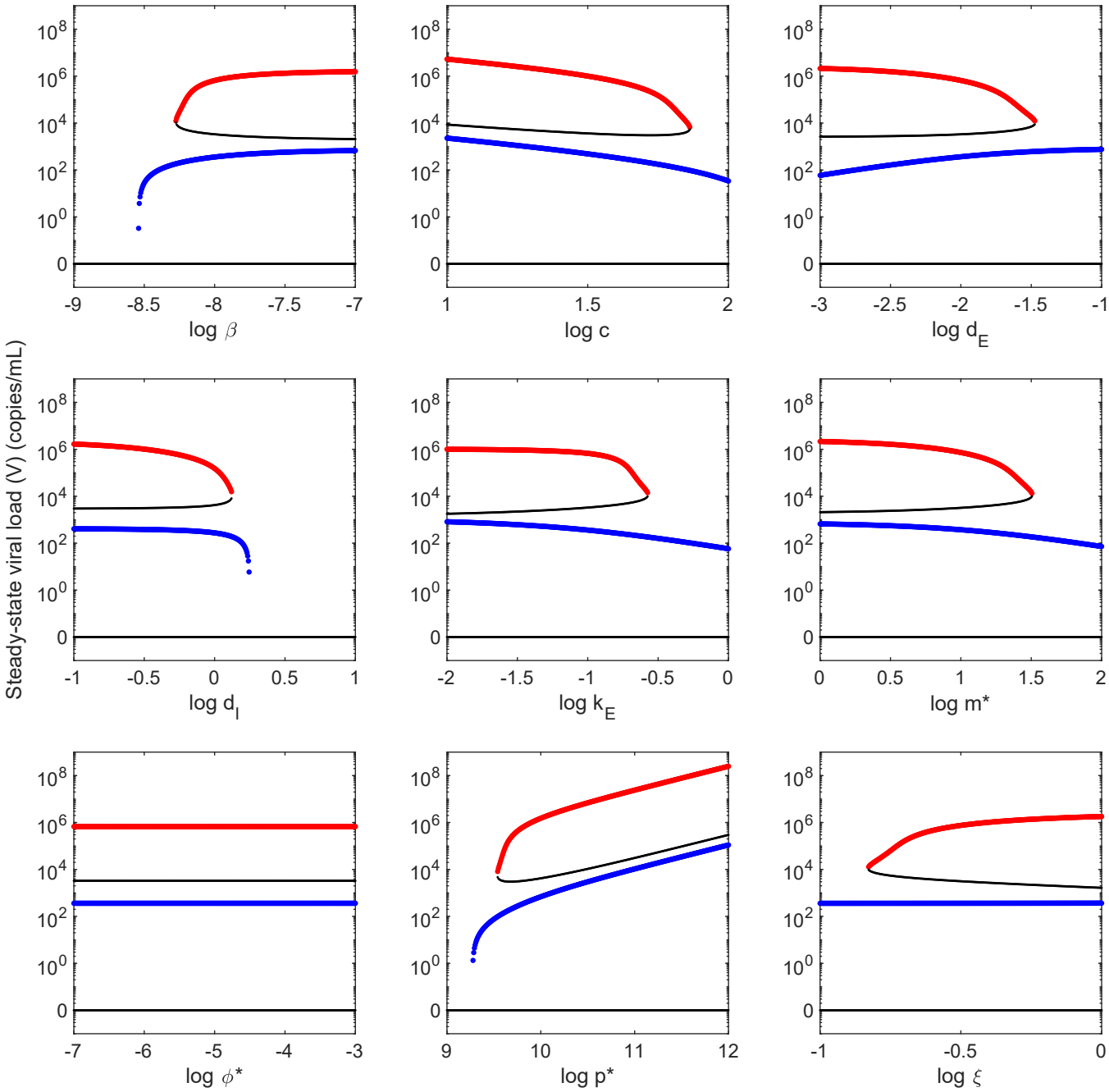

Fig. S3 Bistability and bifurcation diagrams. Steady states of our model (see Text S1) obtained by varying underlying parameters (different panels) one at a time over wide ranges about their values listed in Tables S1 and S2. The stable states of high and low viremia are shown in red and blue, respectively. Black lines represent unstable steady states.

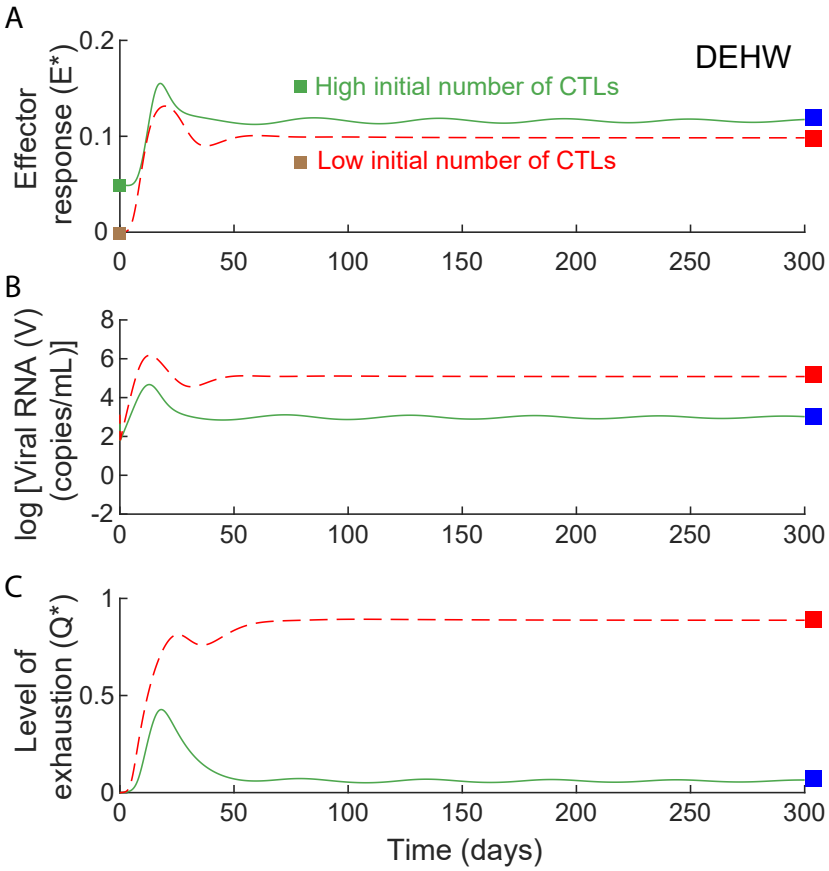

Fig. S4 Model predictions of untreated infection dynamics with high initial CTL numbers. Model predictions of CTL, viral, and exhaustion dynamics for untreated infection show control with high (green) and progression with low (red) initial CTL numbers ($E^*(0)$). All other parameters are the same as those that yield the best-fit to the macaque DEHW (Table S3).

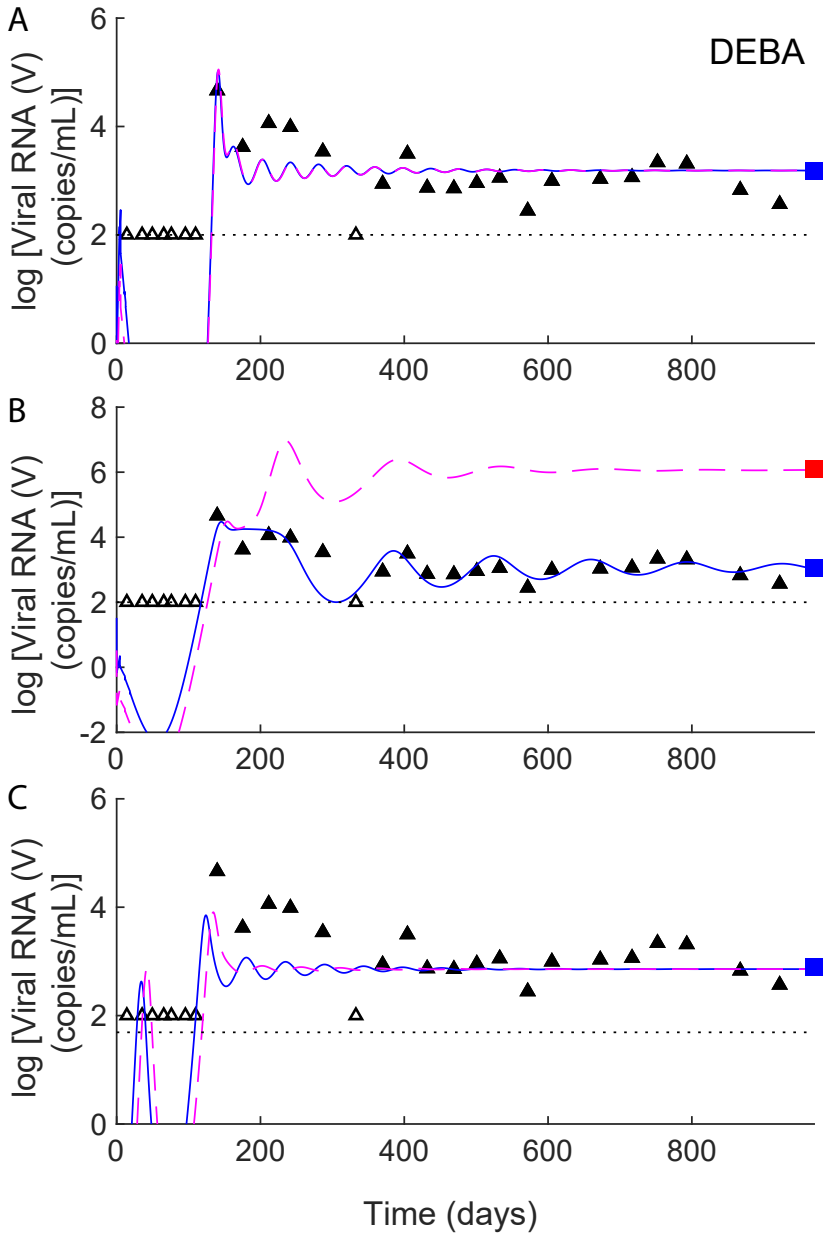

Fig. S5 Models without either antigen clearance or effector elicitation by bNAbs failed to achieve robust fits. (a) Best-fit (blue line) to viral load data (symbols) from the macaque DEBA and corresponding prediction when the initial viral inoculum ($V(0)$) was reduced by $1\ log_{10}$ (magenta) using the other parameters corresponding to DEBA in Table S3. **(b)** Similar fits (blue line) and prediction (magenta) using a variant of our model without bNAb-induced antigen uptake (no fAV term in Eq S6). With our model in (a), the lower viral inoculum did not lead to loss of control. With the latter model (parameters are in Table S5), the lower viral inoculum resulted in lower effector elicitation and hence loss of viremic control. This loss of control is unlike the observations of Nishimura *et al.* ([1]), where the macaques DEMR, DEBA and DEHW were administered viral inocula $1\ log_{10}$ lower than others but still responded to treatment. (c) The best-fit of a model variant without bNAb-induced viral clearance (no AV term in Eq S5; blue line) failed to capture the viral load data (symbols). Specifically, the resurgence of viremia after bNAb clearance and the subsequent dynamics leading to control were not captured by the fits (parameters are in Table S5).

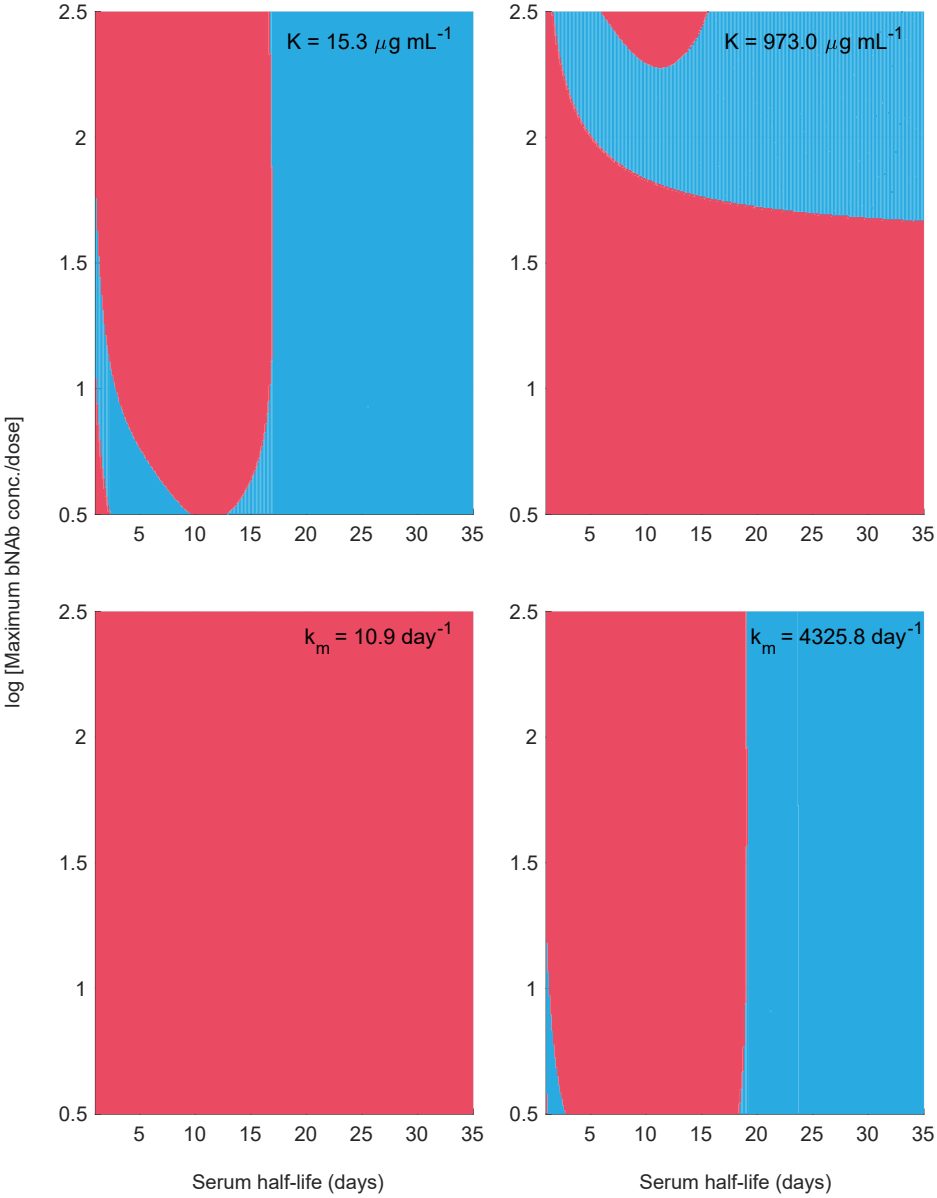

Fig. S6 Sensitivity of phase boundaries to bNAb parameters. The phase diagram of Figure 6 reproduced by varying the parameters K (top) and $k_m = mean(k_1, k_2)$ (bottom). The phase boundaries separating control (blue) and progression (red) vary widely with these parameters. The other parameters are the same as in Figure 6.

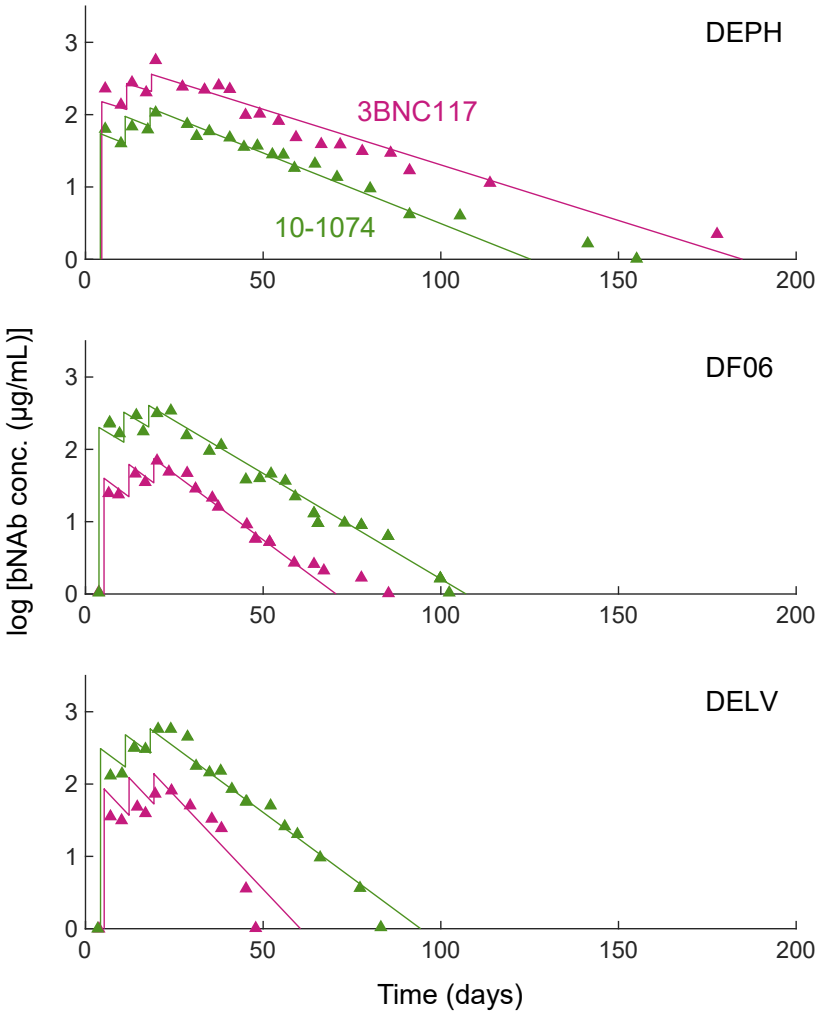

Fig. S7 bNAb pharmacokinetics in non-responders. BNAb pharmacokinetics for non-responders (DEPH, DF06, DELV), obtained by simultaneously fitting Eqs. S6-S7 (lines) to the serum concentration profiles for 3BNC117 and 10-1074 (A_1 and A_2) across the three non-responders ([1]) (Table S6). The average serum half-lives are 11.2 days (range $5.8 - 19.6$ days) for 3BNC117, and 11.3 days (range $8.3 - 15.4$ days) for 10-1074, which are similar to the parameter ranges of the controllers (Figure S1).

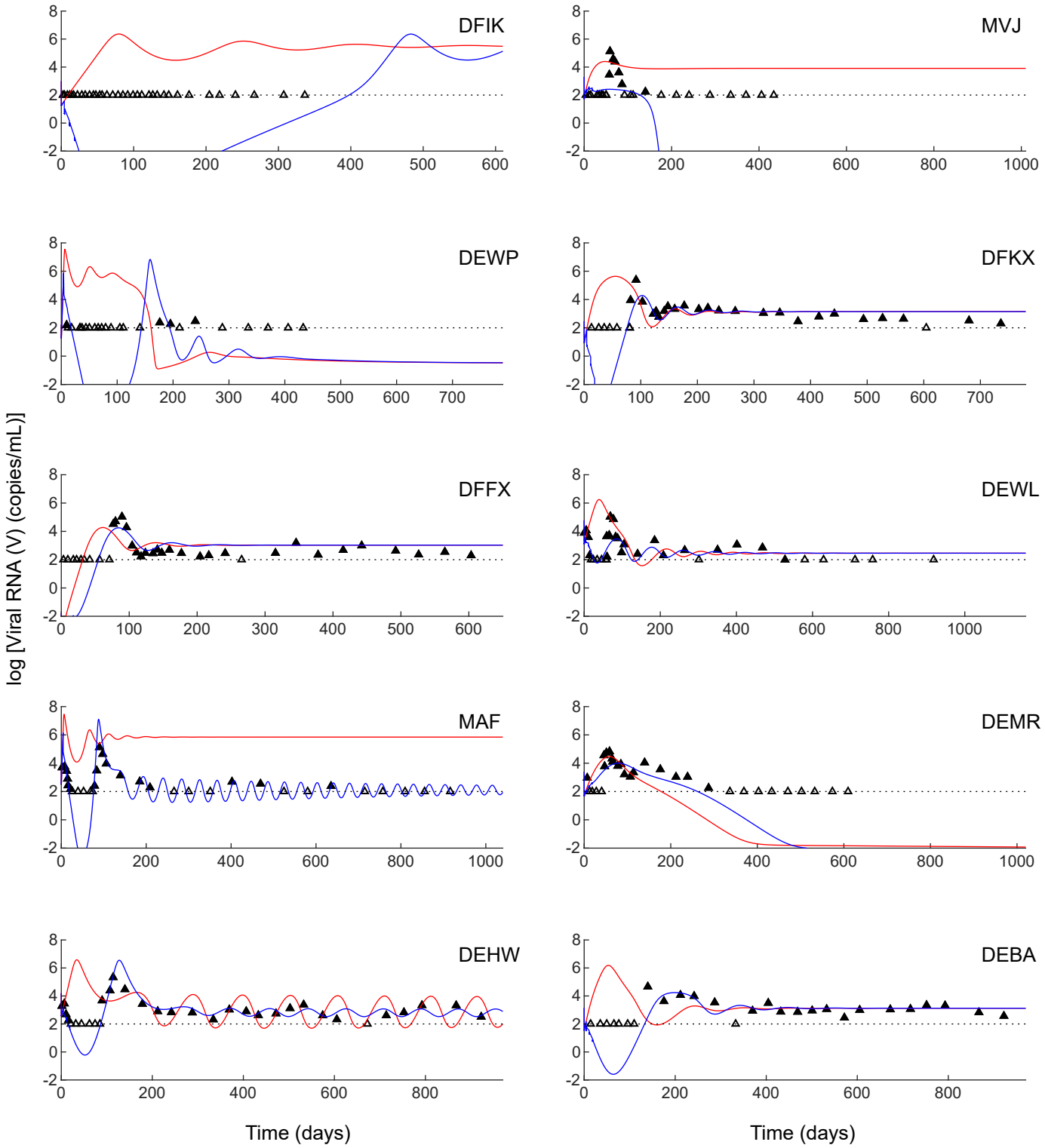

Fig. S8 Alternative model of CTL exhaustion. Fitting with alternative model of CTL exhaustion (Eqs S19-S25) following the procedure outlined in the Text S1 yielded poor fits (blue) to the data (parameters in Table S7). Corresponding predictions without treatment are in red.

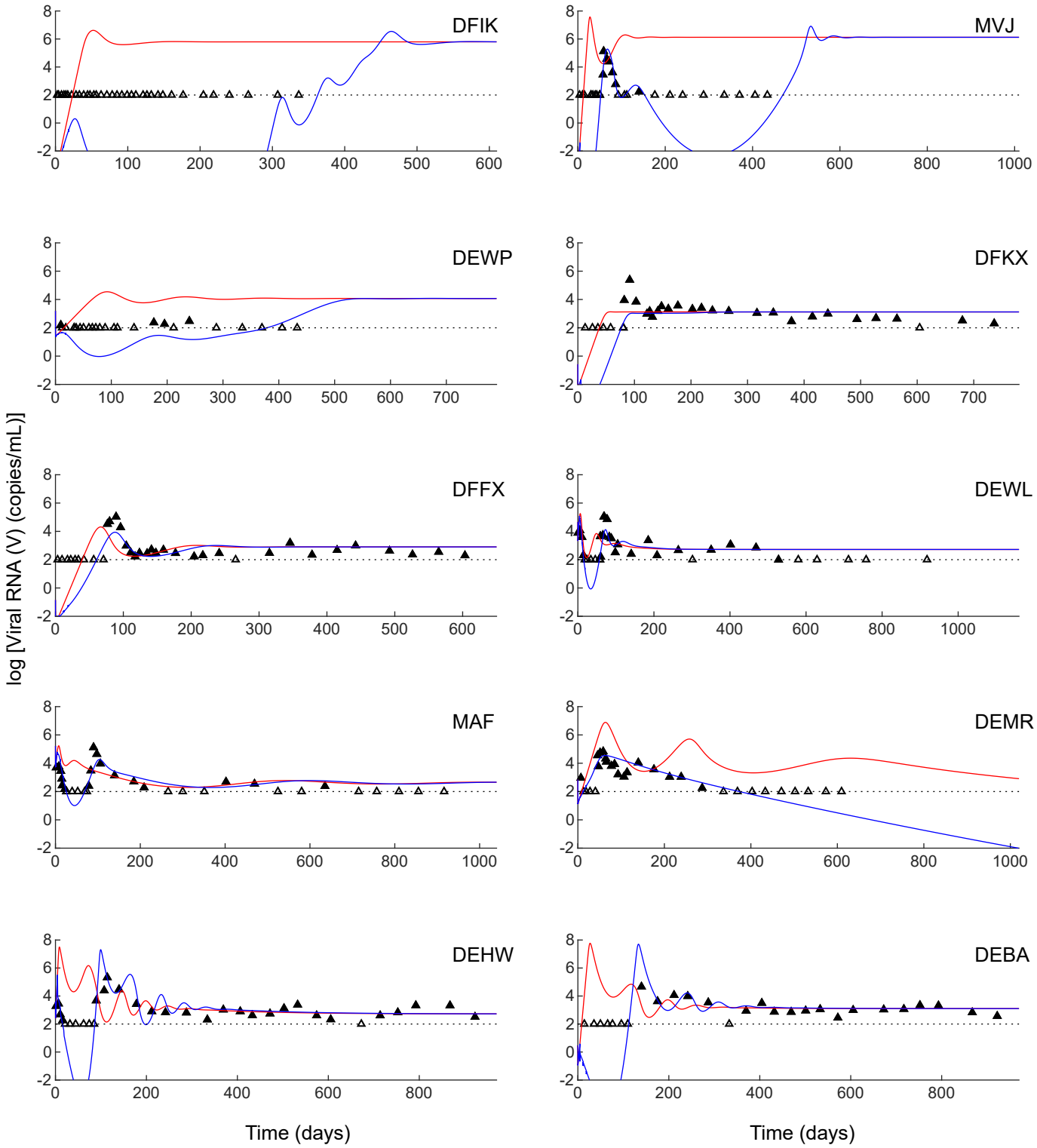

Fig. S9 Hill coefficient, $n = 1$. Fitting our model (Eqs S3-S10) with a Hill coefficient $n = 1$ following the procedure outlined in Text S1 yielded poor fits (blue) to the data (parameters in Table S8). Corresponding predictions without treatment are in red.

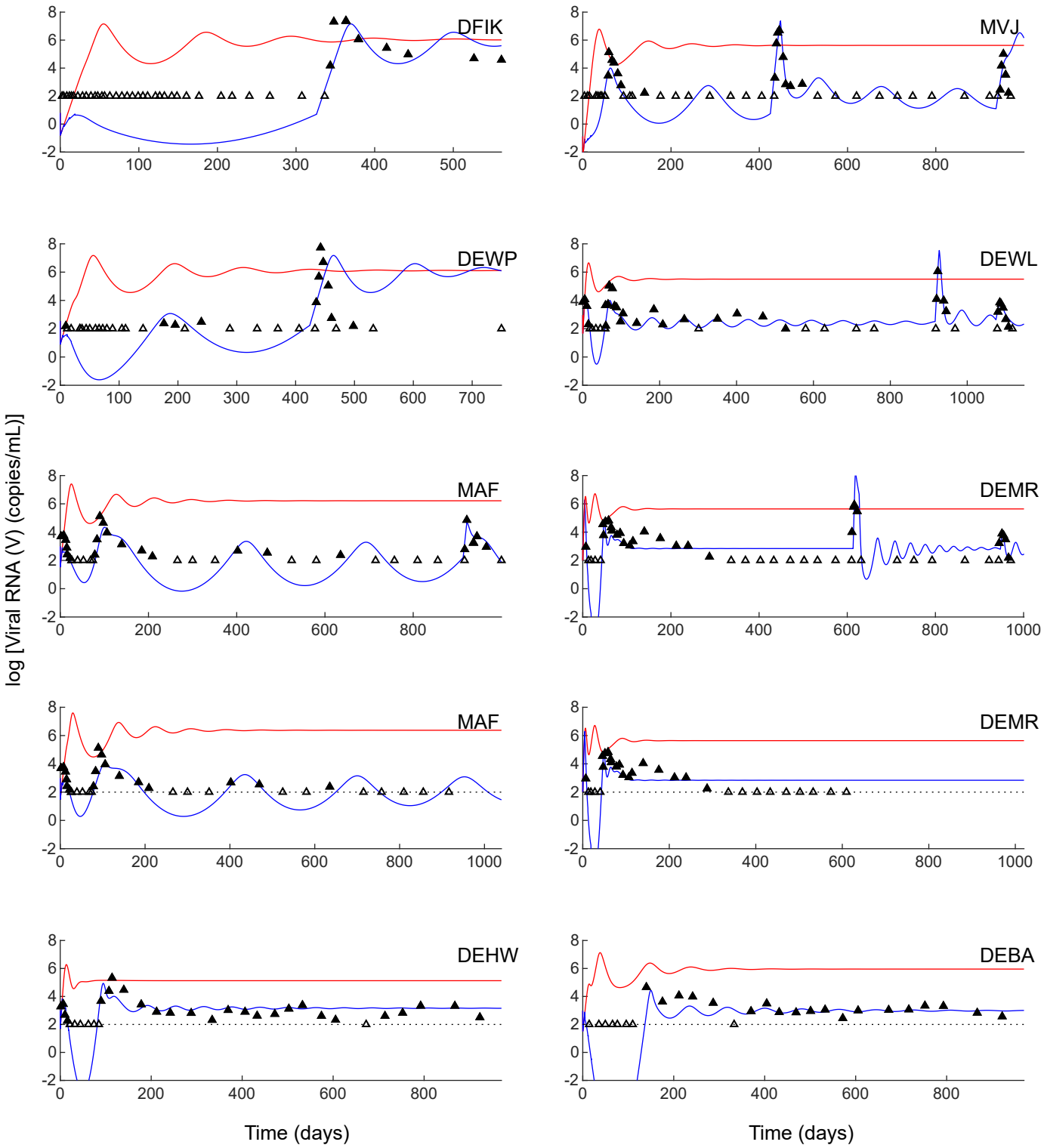

Fig. S10 Hill coefficient, $n = 3$. Fitting our model (Eqs S3-S10) with a Hill coefficient $n = 3$ following the procedure outlined in Text S1 yielded poor fits (blue) to the data (parameters in Table S9). Corresponding predictions without treatment are in red.

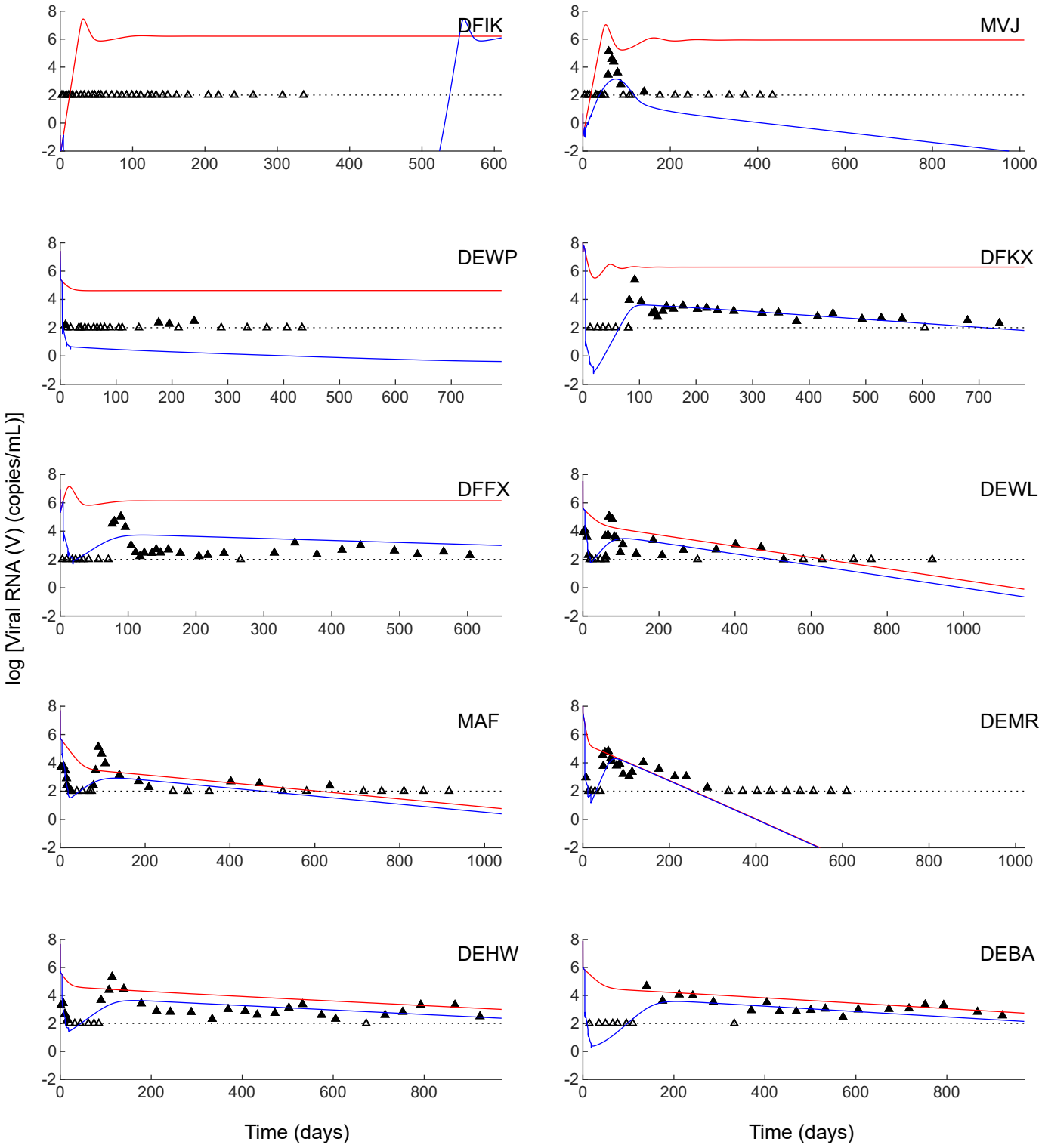

Fig. S11 Absence of CTL response. Fitting with a model without a CTL response (Eqs S26-S30) following the procedure outlined in Text S1 yielded poor fits (blue) to the data (parameters in Table S10). Corresponding predictions without treatment are in red.

Table S1 Model parameters fixed from previous studies.

Symbol	Value	Units	References
d_T	0.01	day^{-1}	3
d_I	0.5	day^{-1}	3
c	38	day^{-1}	7–9
k_E	0.1	day^{-1}	10,11
q_c^*	0.5	-	12
n	4	-	12
d_q	0.1	day^{-1}	12
A_1^{dose}	65000$^{\#}$	μg	1
A_2^{dose}	65000$^{\#}$	μg	1
ε	0.8	-	-

$^{\#}$ Nishimura *et al.,* administer 10 mg/kg of bNAbs to the macaques, and we assume an average body weight of 6.5 kg.

Table S2 Mean population parameters along with their standard deviations estimated in log space by simultaneously fitting our model (Eqs. S3-S10) to data of V, A_1 and A_2 across both untreated macaques and responders (see Text S1).

	$log\ \mu$	σ	Units
$V(0)$	2.2	4.3	virions mL^{-1}
ω_1	0.3	0.3	days
ω_2	0.0	0.1	days
η_1	-1.1	0.6	day^{-1}
η_2	-1.0	0.7	day^{-1}
Vol_1	2.5	1.1	mL
Vol_2	2.8	0.5	mL
k_1	1.5	1.3	day^{-1}
k_2	2.6	1.3	day^{-1}
K	2.1	0.9	μg mL^{-1}
β	-8.0	0.1	virion^{-1} mL day^{-1}
p^*	-9.8	0.2	virion mL^{-1} day^{-1}
m^*	1.0	0.1	day^{-1}
d_E	-2.0	0.3	day^{-1}
ϕ^*	-4.4	1.0	-
ξ	-0.5	0.4	day^{-1}
f^*	-9.1	3.0	virion^{-1} mL day

Table S3 Individual parameter estimates for treated macaques obtained by simultaneously fitting our model (Eqs. S3-S10) to V, A_1 and A_2 across both untreated macaques and responders (see Text S1). Parameters pertaining to effector depletion experiments with anti-CD8α and anti-CD8β antibodies were obtained from individual fits (best fits in Figure 2). The units of all the parameters are the same as in Table S2; ζ_α and ζ_β are dimensionless while θ_m, θ_α, θ_β are in days. (NA - not applicable)

	DEMR	MVJ	DEWP	DEWL	MAF	DFIK	DFKX	DFFX	DEHW	DEBA
$V(0)$	506.42	0.01	2.35	969.05	665.59	0.12	205.86	0.16	1311.13	11.48
ω_1	2.23	2.59	2.07	2.66	2.27	2.09	1.73	2.10	2.49	2.49
ω_2	1.00	1.09	1.02	1.20	1.06	1.24	1.10	1.22	1.06	0.98
η_1	0.26	0.11	0.04	0.09	0.06	0.13	0.07	0.08	0.06	0.06
η_2	0.23	0.28	0.04	0.09	0.07	0.07	0.12	0.20	0.07	0.05
Vol_1	74.90	138.86	336.77	1187.04	1864.01	52.46	521.95	260.89	433.74	262.41
Vol_2	539.42	695.70	1271.71	347.62	464.55	695.10	1292.10	433.17	972.15	1671.88
k_1	3.66	97.42	80.20	2.63	139.42	58.99	55.13	70.54	91.09	433.80
k_2	694.24	2509.54	46.01	202.07	66.98	5.28	1494.26	1096.20	344.08	41.67
K	59.19	148.67	144.49	308.05	141.89	146.72	32.49	69.74	77.64	35.08
β	1.07×10^{-8}	1.04×10^{-8}	1.08×10^{-8}	1.15×10^{-8}	1.02×10^{-8}	1.05×10^{-8}	1.15×10^{-8}	9.64×10^{-9}	1.01×10^{-8}	9.85×10^{-9}
p^*	4.95×10^{9}	7.15×10^{9}	6.92×10^{9}	6.39×10^{9}	6.61×10^{9}	5.95×10^{9}	5.53×10^{9}	5.76×10^{9}	6.41×10^{9}	7.62×10^{9}
m^*	10.58	10.09	10.48	11.13	12.08	10.90	11.45	10.07	10.34	11.28
d_E	8.36×10^{-3}	6.47×10^{-3}	1.24×10^{-2}	1.48×10^{-2}	5.29×10^{-3}	6.73×10^{-3}	1.22×10^{-2}	1.26×10^{-2}	1.23×10^{-2}	2.03×10^{-2}
ϕ^*	5.02×10^{-5}	2.31×10^{-5}	4.15×10^{-6}	5.45×10^{-5}	4.55×10^{-5}	1.46×10^{-6}	1.18×10^{-4}	4.52×10^{-5}	9.09×10^{-5}	8.84×10^{-5}
ξ	0.17	0.21	0.40	0.22	0.20	0.24	0.21	0.21	0.21	0.25
f^*	3.36×10^{-11}	5.49×10^{-8}	5.08×10^{-9}	7.01×10^{-11}	5.45×10^{-10}	2.91×10^{-9}	1.82×10^{-9}	9.69×10^{-10}	3.07×10^{-10}	1.37×10^{-10}
ζ_α	0.33	0.84	0.99	0.40	0.35	0.90	NA	NA	NA	NA
ζ_β	0.56	0.39	NA	0.46	NA	NA	NA	NA	NA	NA
θ_m	11.86	10.68	18.17	5.33	4.73	3.53	NA	NA	NA	NA
θ_α	607.26	436.54	431.86	918.09	916.21	333.23	NA	NA	NA	NA
θ_β	942.50	939.18	NA	1072.86	NA	NA	NA	NA	NA	NA

Table S4 Individual parameter estimates for the ten untreated macaques obtained by simultaneously fitting our model (Eqs. S3-S10) to V, A_1 and A_2 across both untreated macaques and responders (see Text S1).

Macaque	UT1	UT2	UT3	UT4	UT5	UT6	UT7	UT8	UT9	UT10
$V(0)$	52.27	51.93	17.58	3.67	3.22	15.05	1076.07	393.87	243.44	681.12
β	1.06×10^{-8}	1.13×10^{-8}	1.06×10^{-8}	9.61×10^{-9}	9.68×10^{-9}	1.22×10^{-8}	9.74×10^{-9}	1.11×10^{-8}	1.17×10^{-8}	8.86×10^{-9}
p^*	7.83×10^{9}	6.55×10^{9}	7.23×10^{9}	7.85×10^{9}	7.49×10^{9}	5.12×10^{9}	8.56×10^{9}	7.20×10^{9}	7.83×10^{9}	8.07×10^{9}
m^*	11.30	10.66	10.07	10.79	11.83	10.04	10.39	12.06	10.87	11.34
d_E	8.63×10^{-3}	6.93×10^{-3}	7.13×10^{-3}	7.79×10^{-3}	6.57×10^{-3}	8.28×10^{-3}	7.60×10^{-3}	1.23×10^{-2}	4.78×10^{-3}	1.06×10^{-2}
ϕ^*	1.51×10^{-5}	5.44×10^{-6}	1.17×10^{-4}	3.57×10^{-5}	5.85×10^{-5}	1.98×10^{-4}	1.08×10^{-5}	4.49×10^{-5}	2.83×10^{-5}	5.11×10^{-5}
ξ	0.32	0.18	0.54	0.49	0.29	0.43	0.41	0.56	0.33	0.18

Table S5 Individual parameters for macaque DEBA obtained by fitting models without enhanced antigen uptake and subsequent effector elicitation by bNAbs, or without enhanced antigen clearance, to V, A_1 and A_2 simultaneously (see Text S1).

	No antigen uptake (fAV)	No antigen clearance (AV)
$V(0)$	33.03	5.33×10^{-5}
ω_1	1.72	2.31
ω_2	1.50	1.04
η_1	0.06	0.06
η_2	0.05	0.07
Vol_1	237.20	275.63
Vol_2	1902.33	1323.26
k_1	37.50	0.00
k_2	208.54	90.73
K	124.71	1239.35
β	3.05×10^{-9}	1.24×10^{-8}
p^*	9.68×10^{9}	3.79×10^{9}
m^*	7.97	5.87
d_E	8.58×10^{-3}	2.08×10^{-2}
ϕ^*	1.84×10^{-4}	8.40×10^{-5}
ξ	1.04	0.53
f^*	NA	2.74×10^{-7}

Table S6 Individual bNAb pharmacokinetics parameters for bNAb non-responders (DEPH, DF06, DELV), obtained by simultaneously fitting Eqs. S8-S9 to A_1 and A_2 to data from the three non-responders.

Macaque	DEPH	DF06	DELV
ω_1	1.59	2.22	2.27
ω_2	1.18	0.80	1.23
η_1	0.04	0.08	0.12
η_2	0.04	0.07	0.08
Vol_1	430.52	1631.36	761.04
Vol_2	1190.70	323.57	210.55

Table S7 Individual parameter estimates obtained by fitting a model with an alternative description of CTL exhaustion (Eqs S21-25; see Text S1 for details)

	DFIK	MVJ	DEWP	DFKX	DFFX	DEWL	MAF	DEMR	DEHW	DEBA
ω_1	1.71	2.09	1.10	1.51	1.60	2.55	1.36	1.58	1.65	1.72
ω_2	1.14	1.32	1.12	1.48	0.85	0.86	0.84	1.17	1.74	1.19
$V(0)$	9.86×10^{2}	1.98×10^{3}	1.66×10^{2}	2.94×10^{2}	1.53×10^{-2}	6.01×10^{4}	3.57×10^{3}	2.47×10^{3}	1.61×10^{4}	1.42×10^{3}
η_1	0.12	0.10	0.04	0.07	0.10	0.08	0.08	0.26	0.07	0.06
η_2	0.07	0.23	0.04	0.25	0.16	0.10	0.07	0.18	0.07	0.07
Vol_1	58.22	156.47	465.69	618.50	220.32	1644.68	1201.31	53.05	323.90	276.45
Vol_2	764.22	901.37	1250.82	575.51	481.40	258.48	418.49	782.81	1066.82	1272.74
k_1	0.00	0.00	2510.94	0.00	0.00	0.00	30708.34	0.00	0.00	0.00
k_2	1588.14	294.24	162.13	1792.36	383.87	232.45	111.35	181.36	392.91	291.91
K	457.27	798.00	139.83	250.77	2241.92	1516.07	1354.24	1359.91	133.12	81.76
β	1.04×10^{-8}	1.94×10^{-8}	5.53×10^{-8}	1.90×10^{-8}	1.87×10^{-8}	2.00×10^{-8}	4.85×10^{-8}	1.23×10^{-8}	2.03×10^{-8}	1.22×10^{-8}
p^*	2.53×10^{9}	1.87×10^{9}	2.35×10^{9}	2.12×10^{9}	2.17×10^{9}	1.48×10^{9}	2.19×10^{9}	2.27×10^{9}	1.55×10^{9}	2.75×10^{9}
m^*	0.15	12.71	0.56	0.23	2.37	0.06	0.22	0.28	1.25	0.21
d_E	1.35×10^{-2}	2.44×10^{-3}	1.07×10^{-3}	9.04×10^{-2}	1.12×10^{-2}	7.22×10^{-2}	2.01×10^{-2}	2.02×10^{-2}	4.16×10^{-5}	4.25×10^{-2}
ϕ_1^*	2.27×10^{-1}	5.27×10^{-3}	5.53×10^{-7}	2.05×10^{-5}	4.21×10^{-6}	5.32×10^{-6}	9.18×10^{-6}	9.94×10^{-5}	7.58×10^{-6}	3.79×10^{-5}
ξ	0.07	0.07	0.07	0.07	0.12	0.10	0.11	0.08	0.07	0.10
ϕ_2^*	7.48×10^{-6}	5.30×10^{-7}	3.95×10^{-6}	1.55×10^{-3}	4.62×10^{-11}	3.44×10^{-4}	1.27×10^{-4}	6.07×10^{-5}	8.31×10^{-7}	1.08×10^{-4}
f^*	0	0	0	0	0	0	0	0	0	0

Table S8 Individual parameter estimates obtained as in Table S3 but with the Hill coefficient $n = 1$.

	DFIK	MVJ	DEWP	DFKX	DFFX	DEWL	MAF	DEMR	DEHW	DEBA
ω_1	1.31	2.21	0.97	2.00	1.54	1.43	0.85	1.61	2.27	1.61
ω_2	0.89	1.67	1.04	2.43	2.32	1.58	1.08	2.05	1.48	1.43
$V(0)$	7.84×10^{-3}	9.42×10^{-3}	1.58×10^{3}	2.67×10^{-1}	1.42×10^{-1}	4.67×10^{4}	1.68×10^{5}	7.01×10^{2}	3.99×10^{3}	3.00×10^{0}
η_1	0.12	0.10	0.04	0.06	0.10	0.07	0.07	0.28	0.07	0.06
η_2	0.07	0.25	0.05	0.25	0.14	0.09	0.07	0.27	0.07	0.06
Vol_1	64.72	138.60	502.26	627.41	136.64	1783.29	1487.30	47.12	400.49	247.16
Vol_2	641.78	834.52	1088.40	683.72	637.74	317.29	555.65	479.13	1036.00	1444.39
k_1	0.81	0.02	0.35	0.70	0.28	2.92	0.30	0.29	0.47	0.13
k_2	56.94	3027.28	4.21	138.79	55.87	39.10	50.87	65.15	41766.23	1047.63
K	1.85×10^{-5}	6.07×10^{-8}	2.29×10^{-3}	7.54×10^{-4}	0.04	162.74	153.32	35.28	2364.55	36.66
β	8.72×10^{-9}	8.46×10^{-9}	7.23×10^{-9}	9.60×10^{-9}	6.89×10^{-9}	1.80×10^{-8}	7.61×10^{-9}	5.39×10^{-9}	3.10×10^{-8}	6.00×10^{-9}
p^*	4.65×10^{9}	6.94×10^{9}	3.13×10^{9}	3.04×10^{9}	4.26×10^{9}	3.44×10^{9}	5.88×10^{9}	5.20×10^{9}	2.74×10^{9}	8.55×10^{9}
m^*	2.73	41.58	1.81	2.71	6.78	483.58	5180.91	26.52	9.59	0.30
d_E	3.82×10^{-2}	7.74×10^{-4}	2.33×10^{-2}	4.21×10^{-1}	3.51×10^{-3}	8.25×10^{-4}	2.81×10^{-4}	1.63×10^{-5}	2.99×10^{-5}	6.49×10^{-4}
ϕ^*	3.11×10^{-3}	1.62×10^{-3}	3.06×10^{-3}	1.44×10^{-4}	6.59×10^{-5}	5.81×10^{-4}	6.29×10^{-3}	3.72×10^{-3}	1.01×10^{-4}	2.34×10^{-5}
ξ	0.65	0.32	0.02	0.17	0.09	0.19	0.80	0.04	0.06	0.07
f^*	1.93×10^{-4}	2.12×10^{-5}	1.38×10^{-5}	2.67×10^{-9}	4.15×10^{-9}	3.50×10^{-13}	1.24×10^{-10}	8.23×10^{-6}	1.92×10^{-11}	7.18×10^{-8}

Table S9 Individual parameter estimates obtained as in Table S3 but with the Hill coefficient $n = 3$.

	DFIK	MVJ	DEWP	DFKX	DFFX	DEWL	MAF	DEMR	DEHW	DEBA
ω_1	1.78	1.27	1.58	1.32	1.89	1.30	1.80	1.85	1.59	1.72
ω_2	1.78	1.81	1.77	1.88	1.96	1.75	2.31	1.90	2.44	1.97
$V(0)$	6.34×10^{0}	1.33×10^{-1}	3.53×10^{2}	9.87×10^{2}	1.00×10^{3}	9.28×10^{2}	9.99×10^{2}	9.99×10^{2}	1.00×10^{3}	9.53×10^{2}
η_1	0.12	0.13	0.04	0.07	0.10	0.08	0.06	0.21	0.07	0.06
η_2	0.08	0.15	0.05	0.18	0.17	0.09	0.07	0.14	0.07	0.07
Vol_1	80.20	80.30	548.87	608.11	167.20	1630.38	2194.97	117.92	387.75	243.09
Vol_2	601.75	1470.23	1037.82	866.97	564.90	369.15	477.42	832.63	1222.64	1501.78
k_1	54.91	33.41	21.63	75.68	24.69	47.39	46.89	59.66	50.04	58.85
k_2	87.54	377.98	162.26	177.43	1349.73	377.25	64.73	512.79	303.04	505.15
K	3067.59	104.77	570.35	158.55	488.02	1468.32	28.57	453.75	141.67	56.91
β	6.53×10^{-9}	1.13×10^{-8}	4.68×10^{-9}	1.11×10^{-8}	6.45×10^{-9}	1.47×10^{-8}	5.38×10^{-9}	1.44×10^{-8}	1.47×10^{-8}	8.28×10^{-9}
p^*	5.20×10^{9}	4.15×10^{9}	6.82×10^{9}	4.52×10^{9}	5.79×10^{9}	4.45×10^{9}	8.52×10^{9}	8.91×10^{9}	4.32×10^{9}	5.61×10^{9}
m^*	16.26	15.01	28.81	17.39	25.29	17.42	13.23	36.92	13.29	29.18
d_E	1.06×10^{-3}	1.97×10^{-3}	2.74×10^{-3}	8.47×10^{-3}	7.99×10^{-3}	5.30×10^{-3}	1.44×10^{-3}	1.64×10^{-2}	9.84×10^{-3}	8.79×10^{-3}
ϕ^*	2.65×10^{-5}	5.78×10^{-5}	7.59×10^{-5}	1.96×10^{-4}	1.97×10^{-4}	7.21×10^{-5}	1.05×10^{-4}	5.06×10^{-5}	2.58×10^{-4}	3.29×10^{-4}
ξ	1.08	0.21	3.92	1.28	1.64	0.26	0.26	0.52	0.24	1.51
f^*	5.28×10^{-7}	3.22×10^{-8}	3.67×10^{-8}	6.85×10^{-9}	5.92×10^{-9}	1.17×10^{-9}	3.69×10^{-9}	3.29×10^{-10}	9.08×10^{-10}	9.36×10^{-9}
ζ_α	0.99	0.00	0.38	NA	NA	1.00	0.00	1.00	NA	NA
ζ_β	NA	0.67	NA	NA	NA	0.44	NA	0.34	NA	NA
θ_m	30.00	23.16	25.06	NA	NA	10.74	8.36	13.69	NA	NA
θ_α	326.00	425.05	424.00	NA	NA	916.51	913.15	613.24	NA	NA
θ_β	NA	936.50	NA	NA	NA	1074.76	NA	947.50	NA	NA

Table S10 Individual parameter estimates obtained by fitting a model without an explicit CTL response (Eqs S26-S30; see Text S1 for details). Here, d_L was fixed at 0.004 day^{-1}.

	DFIK	MVJ	DEWP	DFKX	DFFX	DEWL	MAF	DEMR	DEHW	DEBA
ω_1	2.03	2.23	1.63	2.11	2.06	1.88	1.76	2.54	1.52	2.02
ω_2	1.50	1.12	1.02	1.69	1.36	2.47	1.24	1.49	1.04	1.20
$V(0)$	1.36×10^{-1}	4.75×10^{0}	2.68×10^{7}	3.22×10^{8}	8.40×10^{6}	3.44×10^{7}	5.11×10^{7}	7.17×10^{9}	4.77×10^{7}	7.89×10^{7}
η_1	0.12	0.11	0.04	0.07	0.10	0.09	0.07	0.21	0.07	0.06
η_2	0.08	0.08	0.05	0.24	0.19	0.10	0.06	0.20	0.07	0.08
Vol_1	77.57	119.51	411.73	666.02	199.69	1154.70	1231.05	126.27	402.65	179.70
Vol_2	600.62	1425.75	977.06	534.87	435.31	354.16	535.88	541.10	1119.65	1328.18
k_1	5.18×10^{3}	9.52×10^{-1}	5.97×10^{-3}	5.32×10^{2}	6.42×10^{1}	7.74×10^{2}	6.67×10^{1}	7.47×10^{0}	3.33×10^{4}	6.63×10^{-1}
k_2	9.25×10^{3}	1.15×10^{2}	1.40×10^{5}	1.15×10^{8}	1.71×10^{4}	5.74×10^{5}	2.01E+13	7.38×10^{8}	6.97×10^{4}	3.90×10^{5}
K	8.27×10^{-12}	1.00×10^{-35}	6.06×10^{-52}	3.67×10^{-27}	6.84×10^{-38}	1.68×10^{5}	8.43×10^{12}	4.04×10^{5}	2.17×10^{3}	2.35×10^{2}
β	1.18×10^{-8}	9.84×10^{-9}	1.04×10^{-8}	2.46×10^{-8}	9.56×10^{-9}	6.06×10^{-9}	4.56×10^{-9}	5.39×10^{-9}	5.78×10^{-9}	3.62×10^{-9}
p^*	4.78×10^{9}	3.67×10^{9}	2.08×10^{9}	4.80×10^{9}	5.47×10^{9}	2.94×10^{9}	3.59×10^{9}	2.27×10^{9}	3.26×10^{9}	5.12×10^{9}
f_L	1.29×10^{-1}	6.37×10^{-2}	3.12×10^{-1}	1.24×10^{-1}	3.09×10^{-1}	5.33×10^{-2}	3.98×10^{-2}	6.18×10^{-2}	2.20×10^{-1}	1.04×10^{-1}
ψ	2.87×10^{-4}	2.39×10^{-4}	2.32×10^{-4}	2.85×10^{-4}	3.35×10^{-4}	2.95×10^{-4}	6.02×10^{-5}	1.83×10^{-3}	3.61×10^{-4}	8.09×10^{-5}
a	1.48×10^{-2}	4.68×10^{-3}	9.90×10^{-3}	3.02×10^{-3}	3.69×10^{-3}	1.21×10^{-2}	3.35×10^{-3}	3.34×10^{-2}	9.75×10^{-3}	3.89×10^{-3}

Supplementary references

1 Y. Nishimura, R. Gautam, T. W. Chun, R. Sadjadpour, K. E. Foulds, M. Shingai, F. Klein, A. Gazumyan, J. Golijanin, M. Donaldson, O. K. Donau, R. J. Plishka, A. Buckler-White, M. S. Seaman, J. D. Lifson, R. A. Koup, A. S. Fauci, M. C. Nussenzweig, and M. A. Martin. Early antibody therapy can induce long-lasting immunity to SHIV. *Nature*, 543(7646):559–563, 2017.

2 Johan Karlsson, Milena Anguelova, and Mats Jirstrand. An efficient method for structural identifiability analysis of large dynamic systems*. *IFAC Proceedings Volumes*, 45(16):941–946, 2012.

3 J. M. Conway and A. S. Perelson. Post-treatment control of HIV infection. *Proc. Natl. Acad. Sci. U.S.A.*, 112(17):5467–5472, 2015.

4 P. Nagaraja, H. K. Alexander, S. Bonhoeffer, and N. M. Dixit. Influence of recombination on acquisition and reversion of immune escape and compensatory mutations in HIV-1. *Epidemics*, 14:11–25, 2016.

5 Narendra M. Dixit, Martin Markowitz, David D. Ho, and Alan S. Perelson. Estimates of intracellular delay and average drug efficacy from viral load data of HIV-infected individuals under antiretroviral therapy. *Antivir. Ther.*, 9(2):237–246, 2004.

6 B. Ramratnam, S. Bonhoeffer, J. Binley, A. Hurley, L. Zhang, J. E. Mittler, M. Markowitz, J. P. Moore, A. S. Perelson, and D. D. Ho. Rapid production and clearance of HIV-1 and hepatitis C virus assessed by large volume plasma apheresis. *Lancet*, 354(9192):1782–1785, 1999.

7 T. Igarashi, C. Brown, A. Azadegan, N. Haigwood, D. Dimitrov, M. A. Martin, and R. Shibata. Human immunodeficiency virus type 1 neutralizing antibodies accelerate clearance of cell-free virions from blood plasma. *Nat. Med.*, 5(2):211–216, 1999.

8 L. Zhang, P. J. Dailey, T. He, A. Gettie, S. Bonhoeffer, A. S. Perelson, and D. D. Ho. Rapid clearance of simian immunodeficiency virus particles from plasma of rhesus macaques. *J. Virol.*, 73(1):855–860, 1999.

9 M. P. Davenport, R. M. Ribeiro, and A. S. Perelson. Kinetics of virus-specific CD8+ T cells and the control of human immunodeficiency virus infection. *J. Virol.*, 78(18):10096–10103, 2004.

10 R. J. De Boer and A. S. Perelson. Quantifying T lymphocyte turnover. *J. Theor. Biol.*, 327:45–87, 2013.

11 O. Hyrien, R. Chen, and M. S. Zand. An age-dependent branching process model for the analysis of CFSE-labeling experiments. *Biol. Direct*, 5:41, 2010.

12 P. L. Johnson, B. F. Kochin, M. S. McAfee, I. M. Stromnes, R. R. Regoes, R. Ahmed, J. N. Blattman, and R. Antia. Vaccination alters the balance between protective immunity, exhaustion, escape, and death in chronic infections. *J. Virol.*, 85(11):5565–5570, 2011.

13 R. Gautam, Y. Nishimura, A. Pegu, M. C. Nason, F. Klein, A. Gazumyan, J. Golijanin, A. Buckler-White, R. Sadjadpour, K. Wang, Z. Mankoff, S. D. Schmidt, J. D. Lifson, J. R. Mascola, M. C. Nussenzweig, and M. A. Martin. A single injection of anti-HIV-1 antibodies protects against repeated SHIV challenges. *Nature*, 533(7601):105–109, 2016.

14 R. Gautam, Y. Nishimura, W. R. Lee, O. Donau, A. Buckler-White, M. Shingai, R. Sadjadpour, S. D. Schmidt, C. C. LaBranche, B. F. Keele, D. Montefiori, J. R. Mascola, and M. A. Martin. Pathogenicity and mucosal transmissibility of the R5-tropic simian/human immunodeficiency virus SHIV(AD8) in rhesus macaques: implications for use in vaccine studies. *J. Virol.*, 86(16):8516–8526, 2012.

15 Y. Nishimura, M. Shingai, R. Willey, R. Sadjadpour, W. R. Lee, C. R. Brown, J. M. Brenchley, A. Buckler-White, R. Petros, M. Eckhaus, V. Hoffman, T. Igarashi, and M. A. Martin. Generation of the pathogenic R5-tropic simian/human immunodeficiency virus SHIVAD8 by serial passaging in rhesus macaques. *J. Virol.*, 84(9):4769–4781, 2010.

16 Bernard Delyon, Marc Lavielle, and Eric Moulines. Convergence of a stochastic approximation version of the em algorithm. *Ann. Statist.*, 27(1):94–128, 03 1999.

17 H. Y. Chen, M. Di Mascio, A. S. Perelson, D. D. Ho, and L. Zhang. Determination of virus burst size in vivo using a single-cycle SIV in rhesus macaques. *Proc. Natl. Acad. Sci. U.S.A.*, 104(48):19079–19084, 2007.

18 N. Chomont, M. El-Far, P. Ancuta, L. Trautmann, F. A. Procopio, B. Yassine-Diab, G. Boucher, M. R. Boulassel, G. Ghattas, J. M. Brenchley, T. W. Schacker, B. J. Hill, D. C. Douek, J. P. Routy, E. K. Haddad, and R. P. Sekaly. HIV reservoir size and persistence are driven by T cell survival and homeostatic proliferation. *Nat. Med.*, 15(8):893–900, 2009.